Journal of
Marine Science and Engineering

MDPI

Review

Research Progress of Archimedes Spiral Hydrokinetic Turbines in Free-Flow Conditions: A Comprehensive Review

Ke Song [1,2,*], Ji Yao [3], Huiting Huan [4], Liuchuang Wei [1] and Qingxue Liu [1]

[1] School of Mechanical and Electrical Engineering, Kunming University, Kunming 650214, China; weiliuchuang@126.com (L.W.); hmxue2000@163.com (Q.L.)
[2] College of Engineering and Technology, Southwest University, Chongqing 400715, China
[3] Faculty of Mechanical and Electrical Engineering, Kunming University of Science and Technology, Kunming 650500, China; yaoji1974@sina.com
[4] School of Mechano-Electronic Engineering, Xidian University, Xi'an 710071, China; hthuan@xidian.edu.cn
* Correspondence: songke@kmu.edu.cn

Abstract

Ocean current energy is abundant, yet its exploitation is severely constrained by the low-velocity conditions typical of most marine environments, where conventional lift-type turbines exhibit poor self-starting capability and low efficiency. This review provides the first comprehensive synthesis of research on free-stream Archimedes spiral hydrokinetic turbines (ASHTs), a class of drag-dominated rotors developed specifically for low-velocity kinetic energy harvesting. A unified classification is introduced, dividing ASHTs into single-blade long-axis (SL-ASHT) and three-blade short-axis (TS-ASHT) configurations. The energy conversion mechanisms, governed by pressure difference and hydrodynamic force synergy within helical passages, are elucidated, and the influence of critical geometric parameters is assessed. For SL-ASHTs, the analysis highlights exceptional self-starting capability (cut-in velocity: 0.1 m/s), a starting torque coefficient of 0.52, a maximum power coefficient of 0.51, and passive yaw adaptability that limits efficiency variation to below 2% over yaw angles of 0–40°. TS-ASHTs feature a compact architecture and higher rotational speed, facilitating direct generator coupling. With variable blade-angle distributions, thin airfoils, and non-uniform gap ratios, the power coefficient reaches 0.312. Performance-enhancement measures, including multi-parameter optimization, ducts, and winglets, deliver power gains of up to 35%, 122%, and 12%, respectively. This review further identifies critical barriers to engineering deployment: sediment erosion, cyclic fatigue, performance degradation under large yaw angles, and wake interactions. Future priorities include multi-objective optimization, advanced materials and flow control, full-scale sea trials, multiphysics coupling, array layout optimization, and hybrid energy system integration. By establishing a coherent classification and performance-evaluation framework, this work demonstrates that ASHTs offer strong potential as core devices for large-scale utilization of low-velocity ocean current and river hydrokinetic energy.

Keywords: ocean current energy; Archimedes spiral hydrokinetic turbine; hydrodynamic performance; key geometric parameters; free-flow

Academic Editors: Hongsheng Dong and Zeshao You

Received: 28 May 2026
Revised: 13 July 2026
Accepted: 30 July 2026
Published: 6 August 2026

1. Introduction

The International Energy Agency (IEA) estimates that the global technically exploitable ocean current energy resource exceeds 1200 TWh per year, equivalent to approximately 5% of the world's electricity demand [1]. The most abundant resources are concentrated in the Asia-Pacific region, along the Atlantic coast of Europe, and on the east coast of North America. In China alone, offshore technically exploitable ocean current energy exceeds 100 GW, representing enormous development potential. As a clean and renewable energy source, ocean current energy can alleviate global energy supply-demand tensions, reduce dependence on fossil fuels, lower carbon emissions, and promote the sustainable development of the marine economy [2,3].

Nevertheless, large-scale commercial exploitation of ocean current energy still faces considerable technical challenges [4]. The mean flow velocity in the vast majority of sea areas is below 1.0 m/s [5,6], which imposes stringent requirements on the design and operation of conventional hydrokinetic turbines. Traditional horizontal-axis hydrokinetic turbines (HAHTs) and vertical-axis hydrokinetic turbines (VAHTs) are primarily designed for high-velocity environments [7]. Owing to their lift-type operation, these turbines exhibit extremely poor self-starting capability under low-velocity conditions and require complex active control systems to maintain efficiency across operating conditions, significantly increasing equipment costs and maintenance difficulty [8]. Moreover, high-speed rotating blades can threaten marine organisms [9,10], limiting the deployment of such turbines in ecologically sensitive areas [11]. These limitations are particularly prohibitive in emerging application scenarios that demand reliable, low-maintenance power extraction from slow currents. For remote island communities, where diesel generators still dominate, a hydrokinetic turbine that can harvest energy from persistent, low-speed ocean currents offers a pathway to continuous, baseload renewable power and energy independence [12]. However, the turbine must self-start and operate stably at low velocity without demanding frequent on-site maintenance, given the high logistical costs of technician dispatch [13]. Underwater autonomous vehicles (AUVs) performing long-duration seabed surveys, pipeline inspections or environmental monitoring require in-situ recharging stations [14]. A low-flow hydrokinetic turbine integrated into a subsea docking platform can greatly extend mission endurance, yet such a system must reliably generate power in sluggish deep-sea currents without complex control machinery, as any maintenance intervention is extremely difficult [15]. Similarly, in marine ranching and offshore aquaculture, continuous power supply is essential for feeding systems, water-quality sensors, and real-time surveillance. Turbines deployed in these settings must not only operate efficiently in gentle, biologically rich currents, but also pose minimal collision risk to farmed and wild marine life [16], a requirement that directly conflicts with the high rotational speeds of conventional designs. Against this backdrop, exploring novel hydrokinetic turbine technologies, tailored specifically for low-velocity free-stream environments, capable of passive self-starting and robust operation with minimal control, and ecologically compatible, has become a core research direction in ocean current energy exploitation [4].

The Archimedes device has a history of over 2000 years [17–19]. Originally used as a water pump, it was adapted for low-head hydropower generation in the late 20th century [18,20]. Driven by the hydraulic head difference between upstream and downstream, these turbines are suitable for small-scale hydropower applications with heads of 1–6.5 m, and they have been gradually popularized owing to their simple structure, fish-friendliness, and low maintenance cost [21–23]. However, traditional potential-energy Archimedes spiral turbines (ASTs) rely on a water level differential and cannot capture the kinetic energy of free flows, widely present in oceans and rivers, which severely limits their applicability [24–26]. In 2015, Stergiopoulou et al. [27] proposed the concept of an Archimedes spiral hydrokinetic turbine (ASHT) operating in free flow, extending the technology from low-head potential-energy generation to free-stream kinetic energy capture. The world's first ASHT was designed, constructed, and experimentally validated, featuring an axis length = 1 m, diameter = 200 mm, pitch = 200 mm. Tests were conducted in a hydraulic channel. Although the paper does not explicitly report a cut-in velocity, the experimental conditions included a stream flow velocity = 1.76 m/s for theoretical validation. Through theoretical derivation and laboratory prototype testing, they verified the feasibility of generating electricity from hydrokinetic energy under free-flow conditions, thereby providing an entirely new technical pathway for exploiting low-velocity ocean currents and river hydrokinetic energy.

The key technological breakthrough of this ASHT lies in its fundamental departure from conventional potential-energy ASTs. ASTs rely on a head difference (gravitational potential energy) across the spiral, requiring a weir or dam to concentrate water at a higher elevation [18,28]. In contrast, the ASHT operates as a zero-head kinetic energy converter: it harnesses the momentum of flowing water (rivers, open channels, tidal currents) without any elevation difference. The horizontal spiral rotor captures kinetic energy through a drag-based mechanism, where the relative velocity between the stream flow and the rotating blades generates torque. This innovation eliminates the need for civil structures such as dams or headrace channels, enabling deployment in virtually any watercourse with sufficient flow velocity. This concept fundamentally redefined the application boundaries of Archimedes technology and marked the start of free-stream ASHT research. Since then, ASHT research has entered a period of rapid development, progressively establishing a technological chain that spans from basic performance verification through multi-parameter optimization to mechanism studies under complex operating conditions.

Compared with conventional HAHTs, ASHTs can self-start at flow velocities. The helical blade configuration reduces tip speed and noise, while the gradually varying flow passages result in extremely low fish mortality, making them ideally suited for low-velocity free-stream environments. Furthermore, ASHTs are characterized by a simple structure, low manufacturing cost, easy maintenance, and the ability to accommodate flow from arbitrary directions without the need for complex yaw devices. These attributes position ASHTs as a highly promising alternative for low-velocity free-flow energy harvesting. It should be noted, while recent review papers have significantly advanced the understanding of AST, their scope has remained largely confined to traditional low-head potential-energy installations. A growing body of references has summarized design parameters, performance optimization, and site-specific considerations for conventional AST, yet the emerging category of free-stream types has been either overlooked or addressed only superficially. For example, YoosefDoost and Lubitz [28] produced the high citation review in the field, it devoted only a single paragraph to hydrokinetic spiral turbines, merely acknowledging their existence without offering any systematic classification and performance comparison. More recent reviews have either overlooked free-stream concepts entirely or mentioned them without substantive engagement. Ubando, et al. [29], for instance, examined sustainable manufacturability solely within the context of conventional low-head designs, giving no consideration to the distinct structural and material demands of free-flow deployment. Sołowiej and Łapiński [21] provided an extensive overview of recent design and operational advances, yet their analysis was strictly limited to the potential-energy AST. Similarly, Godini et al. [30] conducted a detailed review of AST performance parameters but only briefly referenced hydrokinetic turbines in general terms, without specifically discussing Archimedes spiral configurations or their unique free-stream characteristics. Even when the terminology appeared directly, as in the parametric sensitivity analysis by Uniyal et al. [31], the study included "hydrokinetic" in its keywords while focusing entirely on traditional potential-energy AST in enclosed troughs, thereby failing to address the different flow physics of free-stream ASHTs. Table 1 shows the comparison with representative reviews in the Archimedes spiral turbines field. Consequently, no dedicated review has specifically addressed the research progress of ASTs under free-flow conditions. To address this research gap, this paper conducts a systematic and comprehensive review, thereby presenting the first dedicated review that fills the long-standing absence of a summary for free-stream ASHT technology. The review establishes a unified classification framework that divides ASHTs into two principal structural types: single-blade long-axis type (SL-ASHT) and three-blade short-axis type (TS-ASHT), and systematically examines their research progress, performance enhancement technologies, and engineering challenges. The overarching purpose is to sort out the development context of ASHTs since the concept was proposed in 2015, to build a coherent classification and performance evaluation system, and to reveal the intrinsic relationships between geometric parameters and hydrodynamic performance. Through this synthesis, the review aims to provide a clear overview of the current status and technical advances, analyze the hydrodynamic performance and potential of ASHTs for low-velocity ocean current energy exploitation, and offer researchers and engineers a systematic reference and an in-depth understanding of the technology. The specific goals are threefold: first, to clarify the energy conversion mechanism and flow characteristics of the two typical configurations (SL-ASHT and TS-ASHT); second, to quantitatively summarize the influence laws and optimal intervals of key geometric parameters, and to evaluate the effectiveness and applicable scenarios of various performance enhancement technologies; third, to identify the core bottlenecks that currently restrict engineering deployment and to propose targeted future research directions. In terms of scope, this review concentrates on zero-head, kinetic-energy-driven ASHTs operating in open free flows such as ocean currents, rivers, and open channels, and it explicitly excludes traditional potential-energy AST that rely on hydraulic head difference and dam or weir structures. The coverage encompasses structural classification, energy conversion mechanism, geometric parameter sensitivity, performance enhancement methods, and multiphysics characteristics including fluid–structure interaction, sediment erosion, yaw characteristics, and wake behavior. Topics such as generator design, grid-connected control systems, manufacturing process details, and full life-cycle economic analysis are beyond the scope of the paper. The reference surveyed includes major peer-reviewed journal papers and conference proceedings from the emergence of the free-stream ASHT concept in 2015 to middle 2026. The structure of this review is as follows: Section 2 categorizes ASHTs into SL-ASHT and TS-ASHT and explains their working principles. Following this, in Sections 3 and 4 various methods proposed for improving the hydrodynamic performance SL-ASHT and TS-ASHT performance are presented and discussed, respectively. Section 5 discusses the limitations of two ASHTs. Sections 6 and 7 present the conclusions and identifies the core challenges and proposes future directions.

Table 1. Comparison with representative reviews in the Archimedes spiral turbines field.

Reference	Review Scope	Core Focus	Outcome
YoosefDoost and Lubitz [28]	Conventional AST	Design parameters, performance optimization and site-specific considerations of AST.	Devotes only a single paragraph to hydrokinetic spiral turbines, merely acknowledging their existence without systematic classification and performance comparison.
Ubando et al. [29]	Conventional AST	Sustainable manufacturability of AST.	Examines sustainable manufacturability solely for conventional low-head designs, giving no consideration to the distinct structural and material demands of free-flow deployment.
Sołowiej and Łapiński [21]	Conventional AST	Recent design and operational advances of AST.	Analysis is strictly limited to potential-energy AST, and entirely overlooks free-stream hydrokinetic AST concepts.

Table 1. *Cont.*

Reference	Review Scope	Core Focus	Outcome
Godini et al. [30]	Conventional AST	Detailed review of AST performance parameters.	Only briefly references hydrokinetic turbines in general terms, without specifically discussing Archimedes spiral configurations or their unique free-stream characteristics.
Uniyal et al. [31]	Conventional AST	Parametric sensitivity analysis of AST.	Includes "hydrokinetic" in keywords but focuses entirely on traditional potential-energy AST in enclosed troughs.
This review	Free-stream ASHT	Research progress of ASTs under free-flow conditions.	Dedicated review specifically addressing the research progress of ASTs under free-flow conditions.

Systematic Review Methodology

The literature search was conducted across four mainstream academic databases: Web of Science Core Collection, Scopus, ScienceDirect, and Google Scholar, to cover the full range of international research on ASHTs. The search time range was set from January 2015 to June 2026, covering all representative studies since the systematic development of ASHT technology. The search keywords were constructed around the research topic and core content, using the following combined terms: ("Archimedes spiral hydrokinetic turbine" OR "Archimedes screw hydro turbine" OR "spiral horizontal axis hydro turbine" OR "drag-type horizontal axis hydrokinetic turbine") AND ("performance" OR "flow control" OR "structural characteristic" OR "numerical simulation" OR "experimental study").

To ensure relevance and quality, the following inclusion and exclusion criteria were established. Inclusion criteria: Peer-reviewed journal articles and full conference papers with complete research data and reproducible methods. Research focusing on ASHT hydrodynamic performance, structural optimization, flow control design, or engineering application. Studies validated by physical experiments or reliable numerical methods. Exclusion criteria: Studies focusing only on potential-energy Archimedes spiral turbines (ASTs), Archimedes spiral wind turbines (ASWTs) without extending to hydrokinetic scenarios. patents, short abstracts, book chapters, and existing review articles. Duplicated publications, retracted papers, and studies with unverifiable data. Figure 1 shows the PRISMA diagram of the literature screening and classification process.

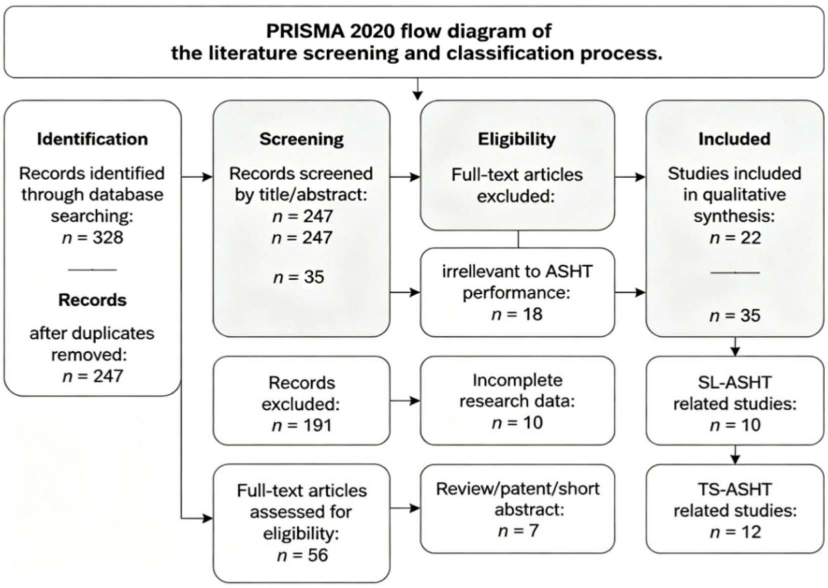

Figure 1. PRISMA diagram of the literature screening and classification process.

2. Classification and Working Principle of ASHTs

The ASHT is a novel horizontal-axis hydrokinetic turbine specifically designed for low-velocity fluid environments. Its distinctive helical blade geometry endows it with significantly superior self-starting capability, yaw adaptability, and environmental friendliness compared with conventional lift-type hydrokinetic turbines. Based on geometric features and design origins, free-flow ASHTs can be divided into two major categories: the SL-ASHT and the TS-ASHT. These two configurations exhibit certain differences in power output, flow behavior and application scenarios.

The hydrodynamic performance of the ASHT is characterized by a set of dimensionless parameters. These include the tip speed ratio (TSR), power coefficient (C_P), torque coefficient (C_M), and thrust coefficient (C_D). The definitions for these key metrics are provided as follows:

$$TSR = \frac{\pi n R}{30 V_0} \tag{1}$$

where V_0, n, and R correspond to the water speed, rotational speed of the ASHT, and rotor radius, with their units given in meters per second (m/s), revolutions per minute (rpm), and meters (m), respectively.

$$C_P = \frac{P}{0.5 \rho A {V_0}^3} \tag{2}$$

$$C_M = \frac{M}{0.5 \rho A {V_0}^2 R} \tag{3}$$

$$C_D = \frac{T}{0.5 \rho A {V_0}^2} \tag{4}$$

where P, M and T correspond to the power output, torque and thrust force. A correspond to the swept area of ASHT's blades, with their units given in watts (W), newton-meter (N·m), newton (N) and square meters (m^2), respectively.

In existing studies, ASHTs have been studied within the low-to-moderate Reynolds number regime. The Reynolds number, defined as $Re = \rho VD/\mu$, serves as a fundamental metric for characterizing the level of flow turbulence. Based on this rotor-diameter Reynolds number, SL-ASHTs fall within the range of 5×10^4–2×10^5, while TS-ASHTs span 7.5×10^4–5×10^5. These ranges correspond to typical ocean current conditions, with flow velocities of 0.3–2.0 m/s.

2.1. Structural Classification and Geometric Features

The SL-ASHT originates from the potential-energy AST. A schematic representation of the SL-ASHT is provided in Figure 2a. The turbine retains the fundamental single-helix blade configuration wound around a central shaft, which is a defining characteristic of Archimedes-type rotors. Common construction materials include carbon steel, stainless steel, and fiber-reinforced composites, chosen to balance mechanical strength, corrosion resistance and weight, especially relevant for prolonged deployment in aquatic environments. Geometrically, the SL-ASHT is characterized by several key dimensionless and dimensional parameters. The aspect ratio (length-to-diameter, L/D) typically exceeds 2.0 and can reach above 5.0 in large-scale designs, enabling a longer flow path and enhanced energy extraction [32,33]. The lead angle θ, which defines the helix pitch relative to the turbine axis, generally lies between 15° and 45°, influencing both the flow passage geometry and the resulting torque characteristics [34]. The blade curvature k, a parameter describing the spanwise blade shape, ranges from 0 to 12 m^{-1}, allowing for optimization between power output and self-starting capability [34,35].

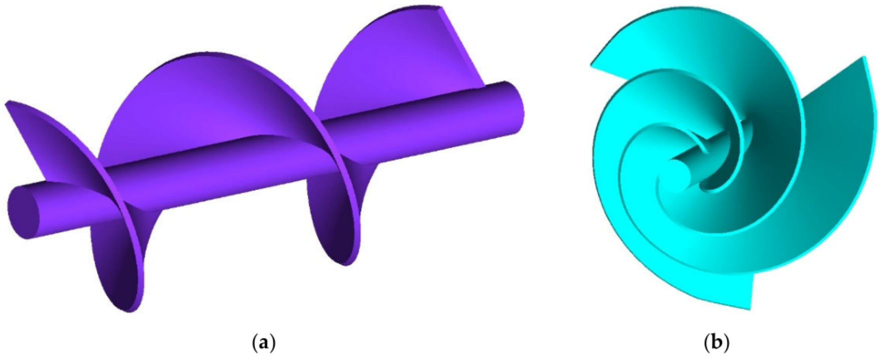

Figure 2. The schematic diagram of two ASHTs: (**a**) SL-ASHT; (**b**) TS-ASHT.

The TS-ASHT represents the most actively researched configuration of the ASHT family, particularly distinguished by its adaptation from the Archimedes spiral wind turbine (ASWT) for compact, lightweight hydrokinetic applications. As illustrated schematically in Figure 2b, its blade structure consists of three independent helical blades evenly distributed around a central shaft at 120° intervals. This three-blade arrangement has been experimentally determined to produce maximum torque and optimal performance. Too few blades reduce the surface area for force conversion, lowering torque, while too many create a solid-wall effect that increases mass and inertia, thereby reducing overall torque [36,37]. The TS-ASHT's geometric parameters are characterized by a low aspect ratio, with mainstream designs adopting an L/D (length-to-diameter) ratio between 0.8 and 1.0 [38]. The blade angle (α) is a critical design variable, typically ranging from 15° to 90°, and configurations can be classified into two categories: fixed-angle (where all three blades share identical angles, 30-30-30, 45-45-45) and variable-angle (where blade angles progressively increase from the first to the third blade, 15-30-45, 30-45-60) [39]. This design flexibility allows the TS-ASHT to be tailored for specific flow conditions and performance requirements. Furthermore, the unique spiral geometry minimizes potential harm to marine life due to its low-speed rotation, while also enabling automatic yaw alignment without external yawing devices, thereby reducing both manufacturing complexity and operational costs. These combined attributes make the TS-ASHT an economically viable and environmentally friendly solution for distributed power generation in low-velocity water bodies.

2.2. Energy Conversion Mechanisms and Flow Characteristics

The SL-ASHT converts energy through the coupled action of pressure difference and hydrodynamic drag within the helical flow passages. Its operating principle is illustrated in Figure 3. Formation of flow passages: Upon entering the enclosed passages formed by the helical blades and the central shaft, the water flow is partitioned by successive blade turns into independent "bucket" units. Establishment of pressure difference: The flow impinges on the pressure side of the blades, creating a high-pressure zone, whereas flow separation on the suction side generates a low-pressure zone; the resulting pressure difference produces a normal force perpendicular to the blade surface. Torque conversion: The normal force is resolved into an axial component and a tangential component; the tangential force generates torque about the central shaft, driving the rotation of the turbine. Momentum transfer: The helical blades progressively convert the axial momentum of the incoming flow into the rotational momentum of the turbine, and the water exits the turbine along the axial direction.

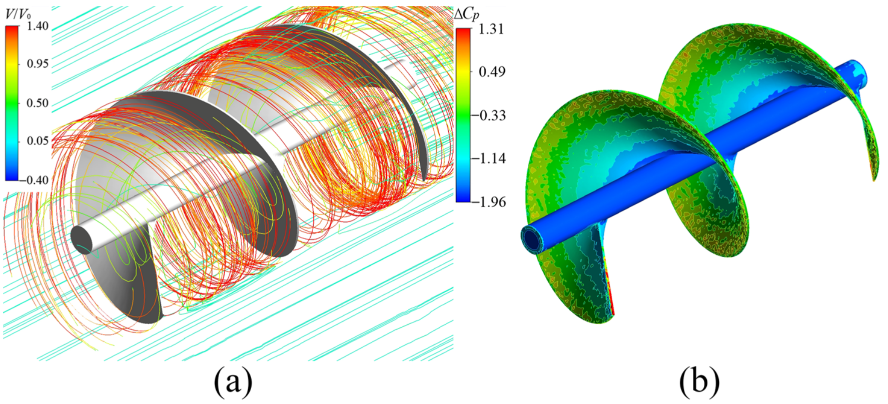

Figure 3. Operating principle of the SL-ASHT: (**a**) flow trajectory inside the helical passage; (**b**) pressure contour on the blade surface.

Unlike the potential-energy AST, which relies on the gravitational work of water contained in the buckets, the free-stream SL-ASHT primarily extracts the dynamic pressure energy of the incoming flow. Numerical simulations indicate that the pressure along the SL-ASHT blade decreases gradually in the axial direction. When the number of turns is excessive, a negative-pressure zone emerges near the tail, leading to increased energy losses. Enlarging the lead angle can effectively reduce the area of the negative-pressure zone and improve the pressure recovery downstream, which constitutes a key mechanism for SL-ASHT performance optimization.

Another unique advantage of the SL-ASHT is its passive yaw capability. Owing to its cylindrical external shape, a self-aligning torque is generated under non-axial inflow conditions, automatically orienting the turbine toward the incoming flow. Zhang et al. [35] demonstrated that within a yaw angle range of 0–40°, the maximum C_P of an SL-ASHT varies by less than 2%, whereas a conventional HAHT may experience an efficiency drop of up to 50% under the same yaw angles. This characteristic eliminates the need for complex active yaw systems and substantially enhances system reliability.

The working principle of TS-ASHT is similar to that of SL-ASHT, making it particularly suitable for low-velocity current environments. The TS-ASHT exploits a hybrid drag-lift mechanism, as its unique helical geometry enables simultaneous generation of axial thrust and tangential lift forces. Its operating principle is illustrated in Figure 4. When water flows axially through the turbine, the pressure side of the blades experiences a high-pressure zone, while the suction side forms a low-pressure region, creating a net pressure difference that generates torque and axial thrust. This pressure-driven torque converts the water's kinetic energy into mechanical rotation. Notably, the ASHT exhibits a low cut-in velocity and maintains stable output torque across a flow velocity range of 0.5–3 m/s, allowing self-starting and efficient operation without auxiliary yaw devices, thereby reducing manufacturing costs.

The flow characteristics around an ASHT are distinct and have been studied using CFD and entropy production theory [39]. The near-wake region is dominated by two primary vortex structures: the tip vortex, which forms due to the pressure difference at the blade tips, and the hub vortex, which results from flow separation and recirculation behind the central shaft. The tip vortex typically exhibits a large, elongated spiral shape that can extend far downstream, while the hub vortex is more intense in configurations with larger blade angles. Energy loss within the flow field is primarily attributed to these vortices, with hub vortices being the dominant contributors to increased entropy production rates, especially for turbines with larger blade angles. The wake behind an ASHT is characterized by a significant velocity deficit, with the lowest velocities observed near the hub and the highest near the blade tips. As the flow moves downstream, the wake gradually recovers its kinetic energy, though the recovery distance is influenced by the blade angle and *TSR*.

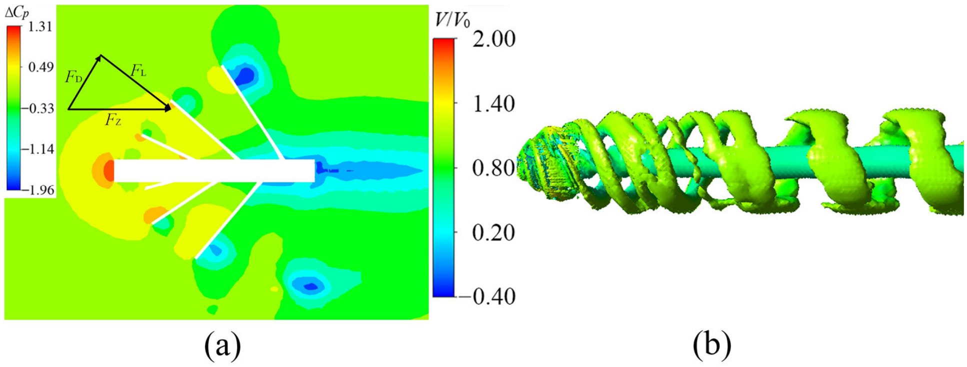

Figure 4. Operating principle of the TS-ASHT: (**a**) schematic of force decomposition; (**b**) vortex distribution.

2.3. Flow Velocity Operating Range

ASHTs are inherently low-flow-velocity energy harvesting devices. Both configurations operate effectively within the low-to-moderate velocity range of 0.3–2.5 m/s, a performance profile distinctly different from the high-velocity-optimized characteristics of traditional lift-type HAHTs. This distinction is directly tied to their drag-dominant power extraction mechanism. For the TS-ASHT, systematic research has established well-defined velocity response patterns. Within the 0.3–2.0 m/s flow velocity interval, the turbine's maximum C_P first rises rapidly with increasing inflow velocity and then approaches a plateau. As flow velocity increases from 0.3 m/s to 2.0 m/s, the corresponding Reynolds number rises from 7.5×10^4 to 5.0×10^5. This increase effectively suppresses boundary layer flow separation and increases the pressure differential across the blade surface, yielding an approximately 5.2% improvement in maximum C_P for typical configurations. Simultaneously, the optimal *TSR* shifts toward higher values as flow velocity increases. Once the Reynolds number exceeds 3.7×10^5 (corresponding to a flow velocity of approximately 1.5 m/s), the performance gain from further velocity increases diminishes markedly, and the efficiency curve enters a plateau phase. This behavior indicates that the effect of flow velocity on turbine performance is most pronounced in the low Reynolds number regime. For the SL-ASHT, no dedicated studies on its velocity-dependent performance characteristics have been reported to date. However, from a structural perspective, the SL-ASHT extends the interaction path between the water flow and the blades, endowing it with excellent self-starting performance and operational stability in the ultra-low velocity range of 0.3–1.0 m/s. This makes it well adapted to application scenarios with persistently low flow speeds, such as deep-water slow currents. The long-axis structure also gives the SL-ASHT a wider optimal *TSR* range, enabling it to maintain relatively mild efficiency fluctuations under variable flow velocity conditions.

2.4. Immersed Depth

To date, no published references have specifically investigated the influence of immersed depth on ASHT performance. All reported numerical and experimental work has been conducted under fully immersed, steady uniform flow conditions. Nevertheless, based on the operating mechanism of horizontal-axis turbines, when a turbine is fully immersed under sufficient water depth, the constraint effect of the free surface is weak and exerts negligible influence on turbine operation. When the water depth above the blade tip is insufficient, however, the low-pressure region on the blade suction side is prone to induce gas precipitation and cavitation inception, while free surface fluctuations can couple with tip vortices to exacerbate flow instability and load fluctuations. Under partially immersed operating conditions, turbine efficiency exhibits pronounced nonlinear behavior. On one hand, the reduced effective swept area causes a linear decline in theoretical power output. On the other hand, blades exposed above the water surface trigger intense flow separation and gas-liquid mixing, introducing substantial additional flow losses; meanwhile, the impact of blades entering the water causes extra energy dissipation. These combined effects drive significant efficiency degradation. Furthermore, the periodic exposure of blade tips above the water surface subjects blades to alternating dry-wet impact loads, which greatly elevates stress levels at the blade root and markedly increases fatigue failure risk. In addition, hydrostatic pressure variations induced by water level fluctuations and free surface scouring accelerate seal wear, raising operation and maintenance costs as well as failure probability.

2.5. Comprehensive Performance Comparison and Applicable Scenarios

Table 2 systematically compares the key performance parameters of the two ASHT types with those of traditional HAHTs and Savonius turbines [32,39–46]. All values are collected from studies with varying geometric scales and test conditions. Cross-type comparisons are for magnitude reference only. Table 3 summarizes the key CFD numerical settings of some representative studies in this field, providing a reference for evaluating the reliability and comparability of numerical results.

Table 2. Comparison of key performance parameters among different hydrokinetic turbines.

Description Parameter	SL-ASHT	TS-ASHT	HAHT	Savonius Turbine
Number of blades	1	3	3	2
Optimal tip speed ratio	1.0–2.0	1.5–2.5	4.0–7.0	0.8–1.2
Maximum C_P	0.35–0.51	0.25–0.35	0.40–0.5	0.20–0.25
Starting C_M	0.3–0.9	0.2–0.5	0.05–0.15	0.15–0.25
Cut-in velocity (m/s)	0.1–0.2	0.15–0.25	>0.7	0.2–0.3
Self-starting capability	Excellent	Good	Poor	Fair
Compactness	Medium	High	Low	Medium

Table 3. Summary of the key CFD numerical settings of ASHTs.

Reference	Turbine Type	Domain Size (D-Based)	Mesh Resolution	Turbulence Model	Boundary Conditions	Inflow Velocity Range	Validation Method
Bouvant et al. [33]	SL-ASHT	Inlet: 5D upstream, outlet: 10D downstream, lateral: 4D from axis	2 million, y + <1	SST k-ω	Velocity inlet, pressure outlet, no-slip wall	1 m/s	Published experimental data
Zhang et al. [34]	SL-ASHT	Inlet: 3D upstream, outlet: 8D downstream	2 million, y + ≈1	SST k-ω	Velocity inlet, pressure outlet, no-slip wall	0.5 m/s	Water flume experiment
Wang et al. [38]	TS-ASHT	Inlet: 4D upstream, outlet: 12D downstream	4 million, y + ≈1	SST k-ω	Velocity inlet, pressure outlet, no-slip wall	0.5 m/s	Published experimental data
Song et al. [39]	TS-ASHT	Inlet: 5D upstream, outlet: 15D downstream	3 million, y + ≈1	SST k-ω	Velocity inlet, pressure outlet, no-slip wall	0.5 m/s	Published experimental data
Badawy et al. [47]	TS-ASHT	Inlet: 3D upstream, outlet: 10D downstream	2 million, y + <1	SST k-ω	Velocity inlet, pressure outlet, no-slip wall	0.5–2.5 m/s	Published experimental data

The SL-ASHT demonstrates exceptional overall performance in terms of self-starting capability and maximum C_P. Its notably high starting C_M and remarkably low cut-in velocity allow it to begin generating power in flow speeds as low as 0.1 m/s, a condition where traditional lift-based HAHTs cannot operate. The optimized SL-ASHT design, as developed and validated by Abbas et al. [32] in an open-channel flow, achieved a C_P of 0.51. This performance is competitive with conventional HAHTs, demonstrating its high efficiency in harnessing kinetic energy from slow-moving water.

The TS-ASHT configuration offers distinct advantages in compactness and operational rotational speed, indicated by its higher optimal *TSR* range of 1.5–2.5. This makes it particularly well-suited for direct coupling with standard generators, thereby eliminating the need for complex and maintenance-intensive gearbox systems. This simplification of the drivetrain is a significant benefit for improving the overall reliability and reducing the mechanical complexity of the power generation system.

A defining characteristic of both ASHT configurations is their exceptionally low cut-in velocities (0.1–0.2 m/s for SL-ASHT and 0.15–0.25 m/s for TS-ASHT), which are substantially lower than the >0.7 m/s requirement of a conventional HAHT. This fundamental advantage renders the ASHT family ideally suited for deployment in energy-poor, low-velocity environments where the mean flow speed is below 0.5 m/s. Such conditions are prevalent in deep-sea currents, making these turbines a highly promising solution for in-situ power generation to support autonomous underwater vehicles (AUVs) and other remote ocean observation platforms.

3. Hydrodynamic Performance of SL-ASHT

The hydrodynamic performance of the SL-ASHT is highly dependent on its distinctive helical geometry. These geometric parameters collectively govern the power output, self-starting capability, and yaw adaptability of the turbine by modifying the flow field distribution and pressure gradients. Previous research has systematically analyzed the impacts of major geometric parameters and uncovered their mutual coupling effects. Table 4 summarizes the influence of these geometric parameters (CFD numerical simulation results). This section analyzes how each critical geometric parameter influences SL-ASHT performance.

Table 4. Summary of the influence of key geometric parameters of the SL-ASHT on hydrodynamic performance.

Geometric Parameter	Investigated Range	Optimal Range	Performance Influence	Key Mechanism
Diameter ratio (D_i/D_o)	0.1–0.6	0.10–0.144	C_P increases linearly as D_i/D_o decreases; a 0.1 decrease yields 12% increase in C_P	Increases effective swept area and reduces hub losses
Blade inclination angle (α)	0–100°	60–90°	C_P first increases then decreases with α; a 10° deviation from the optimum reduces C_P by 5–8%	Affects the flow incidence angle and tangential force component
Blade pitch (p)	100–220 mm	130–220 mm	C_P increases monotonically with p; every 30 mm increase raises C_P by 10%	Reduces inter-blade spillage and wake interference
Shaft length (L)	200–400 mm	320–360 mm	C_P increases monotonically with L; every 100 mm increase raises C_P by 15%	Increases total blade area and energy capture
Blade width (b)	2–6 mm	2–3 mm	C_P increases as b decreases; every 2 mm reduction raises C_P by 5–8%	Reduces flow resistance and blade blockage loss
Lead angle (θ)	15–45°	28–34°	Dominates self-starting performance; every 10° increase raises starting C_M by 40%	Influences blade pitch angle and static torque
Number of turns (n)	1.0–1.8	1.19–1.25	Dominates maximum power output; every 0.2 increase raises max C_P by 8%	Increases total blade area and sweep time
Blade curvature (k)	0–12 m^{-1}	0–8 m^{-1}	Affects bi-directional performance and yaw adaptability; at k = 8 m^{-1}, unidirectional performance improves by 8%	Alters blade pressure distribution and inflow adaptability

3.1. Diameter Ratio (D_i/D_o, Inner Diameter/Outer Diameter)

Among all geometric parameters governing the performance of a SL-ASHT, the diameter ratio (D_i/D_o) is the most influential factor affecting the C_P, with its impact substantially outweighing that of other structural parameters. Bouvant et al. [33] conducted a systematic sensitivity analysis using response surface methodology (RSM) based on a central composite design. Their analysis of variance (ANOVA) revealed that D_i/D_o exhibited the largest F-statistic and the smallest p-value among all design variables, contributing approximately 42% to the variation in C_P. In comparison, the blade inclination angle (α) and the blade pitch (p) contributed only 23% and 18%, respectively. Within the investigated D_i/D_o range (up to 0.6), the maximum C_P increases almost linearly as the diameter ratio decreases. The schematic diagram of SL-ASHT with different D_i/D_o is shown in Figure 5.The full second-order regression model derived from the untransformed response variable predicted an optimal diameter ratio of 0.144, yielding a corresponding maximum C_P of approximately 0.55. In a later multi-objective optimization study by Zhang et al. [34], which aimed to simultaneously maximize both the C_P and the starting C_M, the optimal diameter ratio was found to be approximately 0.133. This value is in close agreement with the 0.144 reported by Bouvant et al. [33], particularly when considering the different objective functions and experimental constraints. The performance enhancement associated with a smaller hub diameter can be explained by several fluid-mechanical mechanisms. First, reducing D_i/D_o increases the effective swept area of the helical blade, allowing the turbine to intercept more kinetic energy from the incoming flow. Second, a smaller hub mitigates flow separation and reduces wake losses in the hub region, where the tangential velocity gradient near the blade root is also diminished. This leads to a more uniform energy extraction and improved overall efficiency. Nevertheless, the diameter ratio cannot be reduced indefinitely. Practical limitations arise from the structural strength requirements of the shaft system and the installation constraints of the power transmission components, such as bearings, seals, and couplings. Thus, while the optimal D_i/D_o from a purely hydrodynamic perspective lies around 0.13–0.14, the final design must balance performance gains against mechanical reliability and manufacturability.

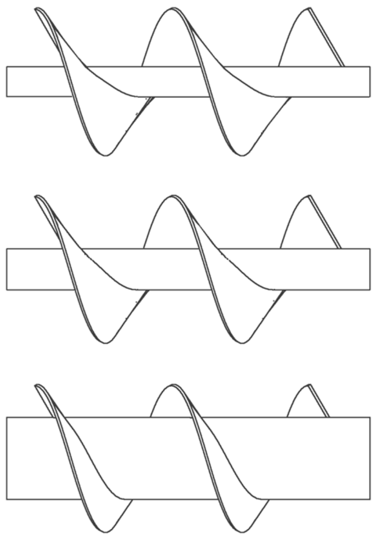

Figure 5. The schematic diagram of SL-ASHT with different D_i/D_o.

3.2. Blade Inclination Angle (α, Angle Between the Blade and the Axis)

Among the geometric parameters affecting the performance of a SL-ASHT, the blade inclination angle (α) with respect to the longitudinal axis is the second most influential factor, after the D_i/D_o. Moreover, α exhibits a strong interaction with D_i/D_o, meaning that the optimal angle is not a fixed value but rather depends on the hub-to-tip ratio and other design variables. The optimal α reported in the literature varies somewhat due to these coupling effects. Bouvant et al. [33] performed a response surface optimization and found an optimal α of approximately 70° (specifically 69.8° in the full regression model and 73.9° in the reduced model) under conditions of D_i/D_o = 0.144–0.10 and a pitch of 160–220 mm. Their results showed that both α and D_i/D_o had the smallest p-values in the ANOVA, confirming their dominant roles and significant interaction. Abbas et al. [32] experimentally investigated three discrete inclination angles (0°, 30°, and 60°) at a flow velocity of 2 m/s. They observed that the C_P increased monotonically with α, reaching a maximum of 0.51 at 60° and a minimum of 0.41 at 0° (as shown in Figure 6). This trend highlights that a higher α allows a larger projected area to intercept the incoming flow, thereby extracting more kinetic energy. Zhang et al. [34] conducted a multi-objective optimization over a wider range of α (60° to 100°). Their results revealed that C_P first increases and then decreases as α rises, with the optimum lying between 80° and 90° depending on the lead angle and number of turns. This non-monotonic behavior is attributed to the trade-off between tangential force generation and flow spillage.

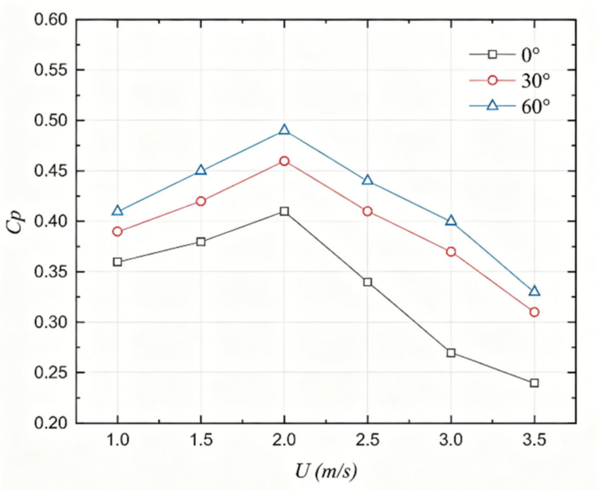

Figure 6. Variation of C_P with different flow velocities at different α [35].

The physical mechanism underlying the influence of α is as follows: the inclination angle determines the local flow incidence angle onto the blade surface, which directly governs the magnitude of the tangential force component responsible for torque generation. A moderate α allows the flow to travel smoothly along the helical blade surface, maximizing the tangential force while minimizing the axial thrust component that opposes rotation. If α is too small (the blade is almost horizontal relative to the axis), the tangential force component becomes insufficient, leading to low output torque and poor self-starting ability. Conversely, if α is too large (approaching 90°), the blade behaves like a nearly vertical wall, increasing flow resistance and spillage losses between adjacent blades, which reduces the effective contact area and diminishes the energy transfer. Importantly, the optimal α increases as the D_i/D_o decreases. A smaller hub (a larger blade area for a given outer diameter) requires a steeper blade inclination to maintain the desired helical pitch angle and to ensure that the flow is guided efficiently across the entire blade surface. This coupling effect is evident in the optimal points reported by Bouvant et al. [33], where the reduced regression model yielded D_i/D_o = 0.10 and α = 73.9°, while Zhang et al. [34] obtained higher optimal α values (85–90°) for turbines with relatively small hub diameters. Therefore, any design optimization must treat α and D_i/D_o as interdependent variables rather than independent ones.

3.3. Blade Pitch (p, Axial Distance Between Adjacent Blades)

The blade pitch (p), defined as the axial distance between two consecutive helical flights, is a critical geometric parameter that governs both the flow capture capacity and the hydrodynamic interaction between adjacent blades. A well-chosen pitch balances the volume of water entrapped in each "bucket" against the leakage and overflow losses, thereby directly affecting the C_P. Experimental and numerical studies have shown that, within a certain range, increasing the blade pitch improves turbine efficiency. Abbas et al. [32] tested three pitch values (100 mm, 115 mm, and 130 mm) for a SL-ASHT under flow velocities from 1 to 3.5 m/s. Their results demonstrated a monotonic increase in C_P with pitch: the configuration with 130 mm pitch yielded a C_P of 0.51, which is approximately 15.9% higher than that obtained with 100 mm pitch (as shown in Figure 7). This improvement is attributed to a larger water-holding capacity per bucket, which reduces the "crowding effect" and minimizes spillage losses as the screw rotates. Concurrently, a longer pitch weakens the wake interference from the leading blade, allowing the following blade to encounter a more uniform flow field and thus extract energy more effectively.

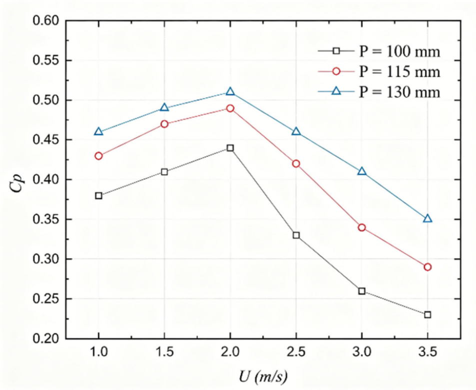

Figure 7. Variation of C_P with different flow velocities at different p [35].

Extending the investigation to a broader design space, Bouvant et al. [33] employed response surface methodology (RSM) combined with CFD simulations (using a 6-DoF UDF method) to optimize four geometric parameters, including blade pitch. Their initial range was 120–200 mm, but the reduced second-order regression model suggested an optimal pitch of 220 mm, yielding a predicted C_P of 0.5137 and a CFD-computed C_P of 0.5515. Notably, the full regression model gave a slightly lower optimum of 159.76 mm. The fact that the optimal pitch from the reduced model lies above the initially tested range indicates that further performance gains may be achievable by increasing pitch beyond typical values, as long as the spiral remains mechanically feasible. However, the relationship between pitch and C_P is not strictly monotonic over an unlimited range. An excessively large pitch reduces the number of active blades per unit shaft length. When the pitch surpasses a certain threshold, the water may pass through the inter-blade gaps without being effectively trapped. Moreover, the torque generated by the turbine may begin to decrease because the pressure difference across the flights becomes insufficient to maintain efficient rotation.

3.4. Lead Angle (θ) and Number of Turns (n)

The lead angle (θ) and the number of turns (n) are two geometrically coupled parameters that jointly define the helical blade profile of a SL-ASHT. For a fixed turbine axial length (L), an increase in the number of turns inevitably leads to a reduction in the lead angle, and vice versa. This inverse coupling leads to distinct roles for each parameter in determining turbine performance.

The number of turns primarily governs the maximum C_P. Under a constant shaft length, a larger n extends the total blade surface area exposed to the incoming flow, thereby enhancing the kinetic energy extraction. Quantitative evidence from Zhang et al. [34] shows that when n increases from 1.0 to 1.8 (with other parameters adjusted within optimization constraints), the maximum C_P rises from approximately 0.34 to 0.46. This trend confirms that increasing the number of turns is an effective way to boost the turbine's maximum power generation capacity. The lead angle, in contrast, dictates the starting C_M, which directly determines the turbine's ability to self-start under low-speed currents. A larger lead angle generates a more favorable pressure distribution along the blade, increasing the circumferential force component at standstill. Experimental and numerical results indicate that raising θ from 22° to 42° can elevate starting C_M from 0.29 to as high as 0.86. This pronounced improvement demonstrates that optimizing the lead angle is the key to achieving reliable startup in deep-water environments where flow velocities are often below 0.5 m/s.

Because n and θ are coupled through the fixed turbine length, an inherent trade-off exists in SL-ASHT design: increasing the number of turns reduces the lead angle, which enhances power output but suppresses self-starting performance; conversely, increasing the lead angle improves startup capability at the expense of reduced maximum power. To navigate this conflict, Zhang et al. [34] employed the NSGA-II algorithm to generate Pareto optimal fronts under different length constraints. For a practical length limitation of 400 mm, the optimal compromise is achieved at n = 1.25 and θ = 34°. This configuration yields maximum C_P = 0.38 and starting C_M = 0.52 that are validated by both the surrogate model and subsequent water flume experiments. Notably, this optimized SL-ASHT can self-start at an extremely low flow velocity of 0.1 m/s while maintaining a high power output, representing a 36.7% increase in maximum C_P and a 143% increase in starting C_M compared to the initial design.

3.5. Blade Curvature (k)

Blade curvature (k), defined as the bending of the blades in the plane perpendicular to the rotor axis, significantly influences the bidirectional energy capture capability and yaw adaptability of the SL-ASHT. Zhang et al. [35] systematically investigated the yaw characteristics of SL-ASHTs with varying curvatures and identified distinct performance trends. For a flat-bladed configuration (k = 0), the turbine exhibits perfect geometric symmetry. Consequently, the maximum C_P is identical for inflow angles of 0° and 180°. Such a SL-ASHT can effectively accommodate inflow angles within a range of ±44°, and its C_P varies by less than 5% over a yaw angle range of 0–40°. As curvature increases to k = 8 m^{-1}, the asymmetry along the flow direction becomes more pronounced. The maximum C_P at 0° inflow improves by 8% compared to the flat-bladed case, but at 180° inflow it drops to 81.8% of the 0° value. The effective operating range narrows to ±40°. When curvature is further increased to k = 12 m^{-1}, the asymmetry intensifies further: the maximum C_P at 0° inflow rises by 12% relative to the flat blade, whereas at 180° inflow it falls to only 68% of the 0° value. The operable inflow angle range shrinks to ±20°. Therefore, for environments with highly variable inflow directions, blades with small curvature (k = 0–4 m^{-1}) are recommended to maintain bidirectional performance. In contrast, for scenarios where the inflow direction is fixed, blades with large curvature (k = 8–12 m^{-1}) can be adopted to enhance unidirectional power extraction.

3.6. Other Geometric Parameters

The shaft length (L) determines the total helical blade area exposed to the flow, thereby affecting the turbine's energy capture capacity. In principle, a longer shaft provides a larger surface for momentum transfer, which can lead to a higher C_P. However, this relationship is not unconditional. An excessively long shaft increases the rotor's moment of inertia, which can deteriorate self-starting capability and reduce responsiveness to flow transients. Furthermore, longer shafts add structural weight and complicate installation.

Interestingly, Bouvant et al. [33], in their response surface methodology (RSM) optimization of a SL-ASHT, found that within their experimental domain (L ranging from 300 to 340 mm), the axle length did not have a statistically significant effect on C_P, suggesting that other geometric factors like the diameter ratio and blade inclination angle are more dominant. Therefore, while a minimum shaft length is necessary to achieve adequate blade area, increasing L beyond an optimal point yield diminishing returns and may introduce mechanical drawbacks.

Blade width (b), defined as the radial thickness of the blade, primarily influences flow resistance and structural integrity. Narrower blades present a smaller obstruction to the incoming flow, reducing hydrodynamic drag and allowing more fluid kinetic energy to be converted into rotational mechanical energy. This trend is empirically supported by Abbas et al. [32], who experimentally and numerically investigated three blade widths (2 mm, 4 mm, and 6 mm) for a SL-ASHT. Their results clearly demonstrated that the C_P increases as blade width decreases. Specifically, the configuration with a 2 mm blade width achieved a C_P of 0.51, which is approximately 8.5% higher than that of the 6 mm blade. This improvement is attributed to reduced flow blockage and lower frictional losses. Nevertheless, the blade width cannot be reduced arbitrarily, as it must maintain sufficient structural strength to withstand hydrodynamic loads, especially at higher flow velocities.

3.7. Special Hydrodynamic Characteristics

Furthermore, the SL-ASHT exhibits several distinctive hydrodynamic characteristics that are not observed in conventional lift-type hydrokinetic turbines. These include a passive self-yawing capability, wide-angle operational adaptability, and exceptional self-starting performance, all of which make the SL-ASHT particularly attractive for deep-sea energy harvesting applications where flow conditions are highly variable and maintenance is challenging.

Zhang et al. [35]. were the first to identify that the SL-ASHT possesses a unique passive self-yawing ability, allowing it to automatically align its axis with the incoming flow direction without requiring any auxiliary yaw control mechanism. This behavior arises from the interaction between the cylindrical rotor surface and the bypass flow around the turbine. When the rotor axis is misaligned with the inflow direction, the asymmetric pressure distribution generates a net yaw moment. This moment drives the turbine to rotate passively until its axis becomes parallel to the flow, thereby minimizing the yaw angle and maximizing energy capture. In contrast, conventional HAHTs typically require active yaw systems to achieve similar alignment, which adds complexity and reduces reliability in deep-sea environments.

For fixed-installation configurations, the SL-ASHT achieves remarkable wide-angle adaptability without any orientation adjustment. When the blade curvature parameter $k = 0$, the turbine is fully symmetric along its axis. Under such conditions, the variation in the maximum C_P remains below 2% over a yaw angle range of 0° to 44°. This performance stability is far superior to that of conventional HAHTs, where a 40° yaw angle typically causes a 50% drop in maximum C_P. Moreover, the SL-ASHT can generate power bidirectionally, delivering nearly identical performance for inflow directions of 0° and 180°. This bidirectional capability makes the SL-ASHT especially suitable for tidal flows and other environments where the current direction reverses periodically, eliminating the need for turbine reorientation.

Self-starting ability is a critical metric for hydrokinetic turbines operating in low-velocity environments, such as deep-sea currents where flow speeds often fall below 0.5 m/s. The SL-ASHT far outperforms conventional lift-type turbines in this regard. An optimized SL-ASHT achieves a starting C_M of 0.52, which is approximately three times that of a

Savonius turbine and six times that of a typical HAHT. Consequently, the cut-in flow velocity can be as low as 0.1 m/s, enabling reliable start-up and operation under the vast majority of deep-sea flow conditions. This exceptional low-velocity performance ensures that the SL-ASHT can consistently harvest energy even in regions with weak or intermittent currents, significantly enhancing the feasibility of in-situ power generation for deep-sea observation equipment.

4. Hydrodynamic Performance of TS-ASHT

Geometric parameters are likewise the core factors determining the hydrodynamic performance of the TS-ASHT, directly influencing its energy capture efficiency, self-starting capability, and vortex structures by modifying the blade-flow interaction and pressure distribution. Existing studies have systematically analyzed the effects of key parameters including blade angle, pitch distribution, airfoil profile and gap ratio. Meanwhile, a systematic optimization framework centered on the logic of "basic geometry-flow field matching-performance synergy" has been gradually established. This section analyzes how each key geometric parameter influences TS-ASHT performance.

4.1. Blade Angle (α)

The blade angle (α), defined as the angle between the blade and the rotational axis plane (as shown in Figure 8), is the most critical geometric parameter governing the performance of TS-ASHT. This angle directly dictates the distribution of normal and tangential hydrodynamic forces on the blades, thereby influencing torque generation, self-starting capability, and even long-term operational durability. Based on the distribution of the blade angle, TS-ASHT configurations are broadly classified into two categories: fixed-angle and variable-angle.

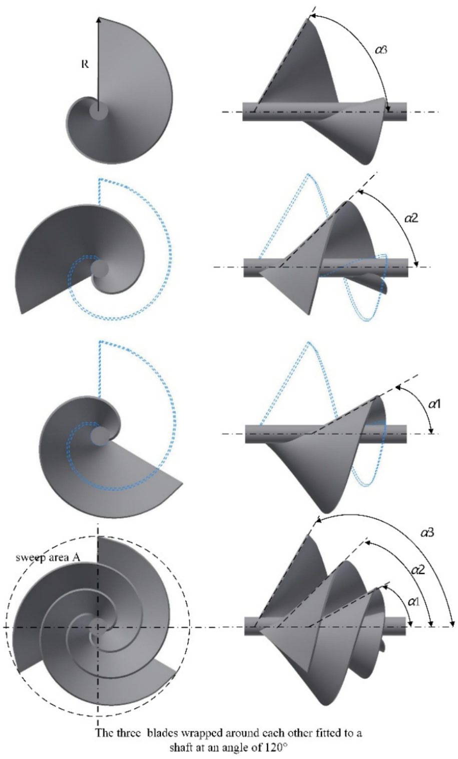

Figure 8. Definition of the blade angle on an ASHT [48].

Fixed-angle configurations, where all blades maintain a consistent angle along the axis, are favored for their structural simplicity and ease of manufacture. Experimental investigations by Monatrakul et al. [49] compared two fixed-angle TS-ASHTs with blade angles of 18° and 21° against a conventional three-blade HAHT. Their results demonstrated that the 21° fixed-angle configuration achieved the highest torque output under free-flow conditions. This superior performance is attributed to the TS-ASHT's drag-driven nature, which enables better self-starting and stable power generation at low flow rates, a condition where lift-driven HAHTs struggle to initiate rotation [50]. In contrast, variable-angle configurations feature a progressively increasing blade angle along the axial direction. This design optimizes energy capture by better matching the local flow velocity distribution across different radial positions. Using numerical optimization, Badawy et al. [47] proposed a variable-angle combination of 25-50-60°, which improved the torque coefficient by 13.2% compared to a conventional fixed 30-45-60° design. Expanding on this, Song et al. [39] systematically evaluated nine TS-ASHT configurations across a wide range of fixed and variable angles. Their findings revealed that the variable-angle configuration 60-75-90 achieved a maximum C_P approximately 14% higher than the optimal fixed-angle case (45-45-45). Furthermore, variable-angle designs with a low angular gradient (15-30-45) exhibited superior self-starting performance, significantly exceeding that of all fixed-angle configurations.

However, blade angle selection also presents a trade-off regarding operational durability. Song et al. [51] demonstrated that the erosion rate of TS-ASHT blades follows a distinct tiered pattern: moderate angles > small angles > large angles. Configurations with moderate angles (30-45-60, 45-45-45) create a synergy between normal impact (which induces plastic deformation) and tangential cutting (which removes deformed material), resulting in the highest erosion rates. Conversely, large-angle blades (75-75-75, 90-90-90) are dominated by near-perpendicular normal impacts, which produce pitting but lack sufficient tangential force for effective material removal, thus exhibiting the lowest erosion. Small-angle blades primarily induce a micro-cutting action with limited plastic deformation, yielding intermediate erosion levels. A detailed comparison is presented in Table 5 (CFD numerical simulation results).

Table 5. Performance comparison of ASHTs with different blade angle configurations.

Configuration Type	Representative Angles	Inflow Velocity Range	Maximum C_P	Starting C_M	Erosion Rate
Fixed angle	30	0.5 m/s	0.161	0.261	Moderate
Fixed angle	45	0.5 m/s	0.214	0.264	Highest
Fixed angle	60	0.5 m/s	0.206	0.172	low
Fixed angle	75	0.5 m/s	0.220	0.142	low
Fixed angle	90	0.5 m/s	0.228	0.133	low
Variable angle	15-30-45	0.5 m/s	0.200	0.311	Relatively high
Variable angle	30-45-60	0.5 m/s	0.235	0.258	Relatively high
Variable angle	45-60-75	0.5 m/s	0.236	0.212	Moderate
Variable angle	60-75-90	0.5 m/s	0.245	0.177	low

4.2. Pitch (p)

The pitch *(p)* of a TS-ASHT is defined as the axial distance over which a blade completes one full revolution. This geometric parameter directly governs the helical curvature of the blade and the cross-sectional area of the flow passage between adjacent blades, thereby playing a critical role in determining the turbine's hydrodynamic performance. Wang et al. [38] systematically investigated nine turbine models with total pitches ranging from 120 mm to 200 mm (while maintaining a constant back-end length of 90 mm and a turbine diameter D = 300 mm). Through computational fluid dynamics (CFD) simulations, they elucidated the influence of pitch on key performance indicators such as the C_P, thrust coefficient C_D, torque coefficient C_M, and wake characteristics.

Among all tested configurations, the turbine with a pitch of 160 mm (D/L = 0.833) achieves the highest energy capture, with a maximum C_P = 0.268 at TSR = 2. This optimum results from balanced flow deceleration and pressure recovery, efficiently converting axial kinetic energy into tangential torque. As pitch increases, the maximum C_P shifts to lower TSRs: from TSR = 2.2 (120 mm pitch) to TSR = 1.8 (200 mm pitch). Thus, larger pitches suit low-velocity environments, while smaller pitches perform better at moderately higher TSRs due to denser blade arrangements. Pitch also affects wake behavior. Smaller pitches (120 mm) cause significant flow blockage, broad low-velocity wake zones, and longer recovery distances. Increasing pitch reduces flow resistance and wake intensity, but exceeding 160 mm leads to excessive blade spacing, reduced C_P, increased turbulence, and higher energy losses (at 200 mm). The C_D generally decreases with pitch. At 160 mm, a slight increase in average C_D (0.743) correlates with better momentum exchange.

4.3. Airfoil Section

The blade cross-sectional airfoil plays a critical role in determining the lift-to-drag ratio of TS-ASHT, primarily by influencing boundary layer separation and the resulting pressure distribution around the blade surfaces. To systematically explore this effect, Badawy et al. [47] transferred well-established airfoil families from aeronautical engineering, namely the Selig (S), Wortmann (FX), and NACA series, into the context of low- velocity water flows. Their computational fluid dynamics (CFD) study, conducted at an optimal gap ratio (GR) of 0.95, compared the hydrodynamic performance of 14 distinct airfoil profiles. The results demonstrated that thin airfoils consistently outperform thicker ones under such flow conditions, due to their ability to maintain a more favorable pressure gradient and delay adverse separation.

Among the Selig (S) series, the S1091 airfoil, characterized by a maximum thickness of 5.1% and a maximum camber of 5.7%, emerged as the best performer, achieving a maximum C_P of 0.26. Its high-lift characteristics are particularly pronounced at low TSR (<1.5), making it suitable for starting torque and low-flow-velocity conditions. Within the Wortmann (FX) series, the FX66-H80 airfoil (maximum thickness 8%, maximum camber 2.5%) delivered the maximum C_P of 0.26, exhibiting stable performance across medium to high TSRs (1.5–2.5). This stability is attributed to its well-balanced pressure distribution that suppresses flow separation over a wide operational range. The NACA series provided the most substantial performance gains. Among the five profiles tested (NACA4401, 4403, 4405, 4407, and 65107), the NACA4401 airfoil, featuring an extremely low thickness of only 1% and a camber of 4%, achieved the maximum C_P of 0.312 at a TSR of 2. This represents a relative increase of 25.3% compared to the conventional TS-ASHT and a 4% improvement over the modified TS-ASHT with the optimal gap ratio alone. Specifically, the thin blade section generates a significantly larger static pressure difference across the rotor: a pronounced low-pressure zone develops on the suction side and downstream of the turbine, while a high-pressure region persists on the pressure side. This enhanced pressure differential, combined with the formation of a broad low-velocity wake downstream, increases the rate of change of momentum of the water current. Consequently, the TS-ASHT (airfoiled type) with NACA4401 blades converts kinetic energy more efficiently than both the conventional and the gap-optimized designs, confirming that airfoil tailoring at low velocity is a highly effective strategy for improving turbine performance.

https://doi.org/10.3390/jmse14151449

4.4. Blade Gap Ratio (GR)

The blade gap ratio (*GR*) is defined as the ratio of the axial spacing between the second and first blades (S2/S1), and it directly governs the degree of flow field interference between upstream and downstream blades. Badawy et al. [47] systematically investigated seven *GR* configurations ranging from 0.85 to 1.15 under a fixed total pitch (2S = 70 mm). At *GR* = 0.95 (corresponding to S1 = 35.88 mm and S2 = 34.12 mm), the maximum C_P reached 0.3008 at a *TSR* of 2. This represents a 20.8% improvement compared to the conventional equal-spacing design (*GR* = 1, S1 = S2 = 35 mm). Across the entire *GR* range from 0.85 to 1.15, the variation in C_P remains within less than 1%, indicating good robustness of the turbine performance to moderate changes in blade spacing. When *GR* falls below 0.85 or exceeds 1.15, the flow interference between upstream and downstream blades intensifies significantly, causing the C_P to drop by more than 3% relative to the optimum. The non-uniform spacing design ($GR \neq 1$) effectively mitigates the adverse effects of the upstream blade wake on the downstream blade. This results in a more uniform flow distribution through the blade passages and reduces vortex-induced losses, thereby enhancing overall energy conversion efficiency. These conclusions highlight that a slightly compressed downstream spacing (*GR* = 0.95) offers the best hydrodynamic performance for the TS-ASHT.

4.5. Yawed Flow

Based on the comprehensive analysis presented by Song et al. [39], yawed inflow conditions impose a pronounced detrimental effect on TS-ASHT performance. As illustrated in Figure 9, the C_P exhibit a steep decline with increasing yaw angle. Quantitatively, for every 10° increase in yaw angle, the C_P decreases by approximately 25%, while the C_D drops by about 19%. This degradation arises from two primary hydrodynamic mechanisms: first, the axial projected area of the rotor diminishes as the yaw angle grows, reducing the effective kinetic energy available for conversion; second, yawed flow induces a spanwise velocity component that does not contribute to torque generation but instead promotes flow separation and turbulence, particularly at the upstream end of the elongated rotor shaft. When the yaw angle exceeds 50°, most TS-ASHT configurations yield negative C_P values, indicating that the turbine can no longer extract net power from the flow and instead consumes energy to maintain rotation.

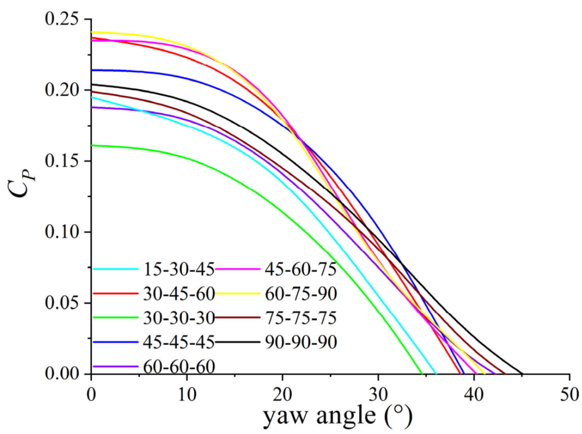

Figure 9. C_P versus yaw angle curves for different ASHTs (Reproduced from [39], with permission from Elsevier).

Beyond these general trends, the yaw adaptability of TS-ASHTs varies considerably with blade angle design. Configurations featuring larger blade angles (the fixed-angle 90-90-90 design) exhibit superior resilience to yaw misalignment. Specifically, the 90-90-90 TS-ASHT maintains a positive power output even at a yaw angle of 45°, a direct consequence of enhanced flow interaction and the ability of steep blades to capture momentum from the oblique inflow. Furthermore, fixed-angle blade configurations consistently outperform variable-angle counterparts under yawed conditions. According to the paper's findings, fixed-angle TS-ASHTs possess an effective yaw angle range that is approximately 15° wider than that of variable-angle designs. This advantage is attributed to the geometric uniformity of fixed-angle blades, which provides more stable pressure distributions and reduced asymmetrical loading when the incoming flow is skewed. In contrast, variable-angle configurations, despite achieving higher maximum C_P in axial flow, suffer from earlier onset of flow separation and vortex shedding under yaw, thereby limiting their operational envelope.

Another critical consequence of yawed flow is the alteration of the wake structure downstream of the TS-ASHT. Yawed inflow causes the wake to deflect laterally and become distorted, creating an asymmetric and highly turbulent region behind the turbine. Unlike HAHTs, whose wake width narrows with increasing yaw angle, the TS-ASHT's wake width remains relatively unchanged due to its greater axial length. While this characteristic mitigates the reduction in projected area, it also prolongs the persistence of large-scale vortices and velocity deficits in the far wake. Such wake deflection and distortion intensify performance fluctuations for any downstream turbines placed in an array, as the incident flow angle and turbulence intensity vary spatially and temporally. Quantitatively based on entropy production theory, the total entropy production rate in the wake region increases by approximately 17% per 10° increment in yaw angle, reflecting a significant rise in turbulent dissipation. When the yaw angle reaches 45°, the asymmetric wake structure causes the local maximum entropy production rate to be 62% higher than that under axial inflow [39].

4.6. Performance Enhancement Techniques

To overcome the energy conversion efficiency bottleneck of the TS-ASHT, researchers have developed various performance enhancement techniques. Table 6 summarizes some of the TS-ASHT performance enhancement techniques (CFD numerical simulation results).

Table 6. Comparison of the TS-ASHT performance enhancement techniques.

Technology Type	Optimal Parameters	Power Increase	Thrust Change	Main Advantages	Main Challenges	Applicable Scenarios
Multi-parameter synergistic optimization	GR = 0.95 + NACA4401 airfoil	25.3%	+8.2%	No additional devices, low cost	High design complexity	Universally applicable
Multi-parameter synergistic optimization	L = 168.921 mm, α = 51.341°, D = 245.645 mm	35%	/	No additional devices, low cost	High design complexity	Universally applicable
Duct/Diffuser	Inlet contraction ratio = 1.68, outlet contraction ratio = 1.36	122%	+110%	Large performance gain, mature technology	Large size, sensitive to yaw	Rivers, irrigation canals
Winglet	Winglet angle = 135°, winglet height ratio = 12%	≥12%	+14.4%	Compact size, does not affect installation space	Large load fluctuations	Deep-sea AUV power supply, miniaturized equipment

A duct/diffuser is a convergent-divergent flow-guiding device installed around the periphery of a turbine (In this review, the C_P of every ducted ASHT model is uniformly defined with the swept area of the internal turbine rotor as the reference area, excluding the frontal area contributed by the duct component). Its primary function is to accelerate the incoming flow by constricting the flow passage, thereby increasing the flow velocity through the turbine rotor. This velocity augmentation directly enhances the input power to the turbine. The underlying principle relies on the Bernoulli effect: as the flow area decreases, the fluid's pressure energy is converted into kinetic energy, resulting in a substantially higher effective flow velocity across the turbine blades. The performance benefits of ducted configurations have been well documented. For instance, Monatrakul et al. [49] reported that adding a duct to a TS-ASHT can increase its torque by 15.15% to 37.89%. Similarly, Song et al. [52] demonstrated that an optimally designed duct can boost the C_P of a TS-ASHT by up to 122%. Figure 10 visually supports these findings by comparing the pressure distribution around a bare TS-ASHT and a ducted TS-ASHT. The ducted version exhibits a larger pressure difference between the pressure and suction surfaces, which directly contributes to its higher C_P. This flow-concentration technology has also proven highly effective in wind energy applications, particularly with Archimedes spiral wind turbines (ASWT) [53–56]. Refaie et al. [57] applied a wind-lens technique (a form of duct) to an ASWT and achieved a C_P of 0.49, 2.1 times that of a conventional, non-ducted configuration. This success offers an important reference for further optimizing the duct technology used in TS-ASHTs. Nevertheless, the adoption of duct technology involves trade-offs [58]. While it is especially suitable for environments with steady, predictable flows and ample installation space, such as rivers and open channels, its drawbacks must be considered. These include an increase in the axial dimensions and overall structural weight of the turbine unit.

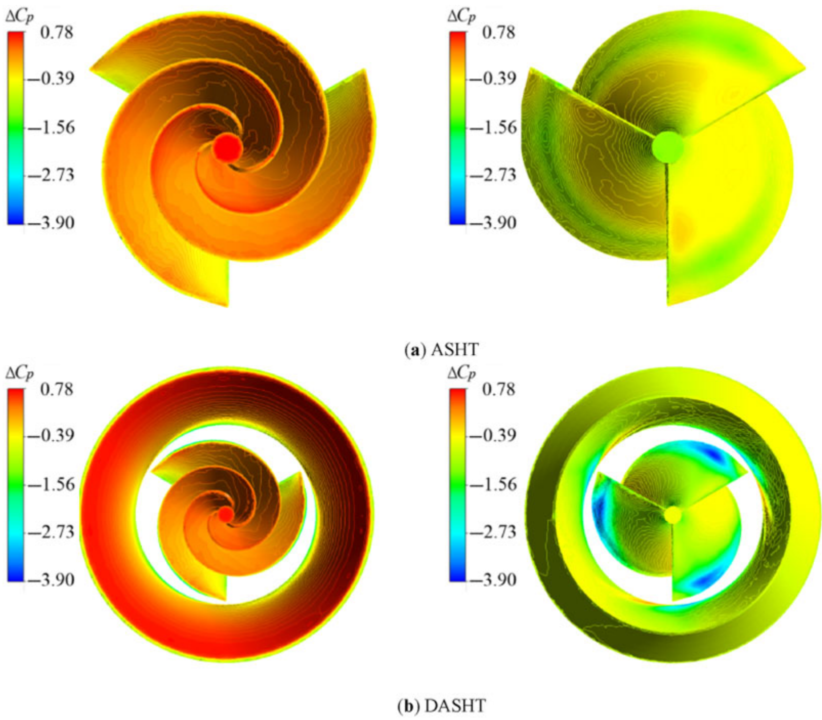

Figure 10. Pressure distribution on the ASHT's and ducted ASHT's pressure side and suction side (Reproduced from [52], with permission from Elsevier).

In a TS-ASHT, blade-tip vortices represent a primary source of hydrodynamic energy loss. This phenomenon arises from the pressure gradient between the pressure and suction sides of the blade: the higher pressure on the pressure side drives flow around the blade tip toward the lower-pressure suction side, thereby generating a helical tip vortex. This vortex dissipates a portion of the kinetic energy from the incoming water flow, reducing the turbine's overall power extraction efficiency. To mitigate such tip losses, Song et al. [59] were the first to systematically apply winglets to TS-ASHTs and investigate their parametric effects. Using computational fluid dynamics (CFD), they examined winglet angles ranging from 60° to 150° and height ratios from 4% to 16%. Figure 11 shows the pressure distribution near blade at fixed winglet height ratio ofh/R = 12% and different winglet angles. Their findings reveal a clear performance threshold: only winglet angles greater than 90° yield positive gains in the C_P. Conversely, angles below 90° increase aerodynamic thrust and reduce C_P, making them detrimental to turbine performance. The optimal configuration identified is a winglet angle of 135° combined with a height ratio of 12%, which produces a minimum increase in C_P of 12.0% compared to the original TS-ASHT without winglets.

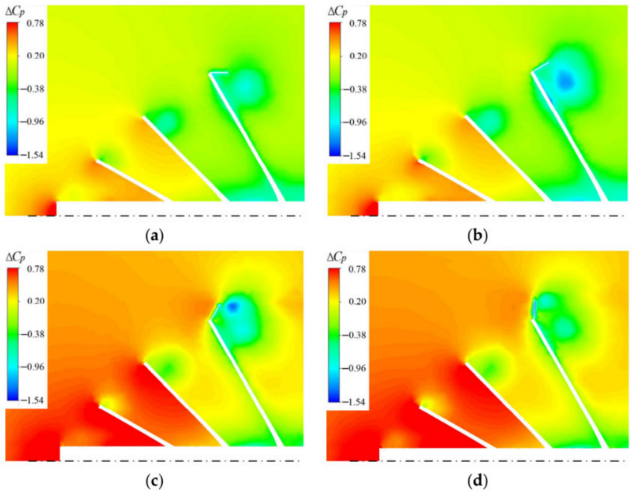

Figure 11. Pressure distribution near blade at fixed winglet height ratio of h/R= 12% and different winglet angles [58]: (**a**) 60°; (**b**) 90°; (**c**) 120°; (**d**) 150°.

The performance improvement stems from two complementary mechanisms. First, the winglet effectively suppresses the strength of the blade-tip vortex, accelerating its downstream dissipation and thereby reducing tip-related energy losses. Second, the winglet enlarges the effective swept area of the blade, allowing the turbine to capture kinetic energy from a larger cross-section of the flow. However, these benefits come with a notable trade-off: winglets substantially increase load fluctuations. Under the optimal configuration, the fluctuation amplitude of the C_P reaches 3.86 times that of the original winglet-free turbine, and the fluctuation amplitude of the C_D reaches 3.65 times. Such intensified cyclic loading can accelerate blade fatigue damage, particularly at the blade root where stress concentrations are highest.

4.7. Multiphysics Characteristics

During operation, the hydrodynamic loads cause elastic deformation and vibration of the blades, which in turn alter the flow field structure, resulting in a fluid-structure interaction (FSI) effect. Song and Kang [60] performed a one-way FSI analysis on two ASHTs at 0.5 m/s and reached the following key conclusions: (1) The maximum stress is concentrated at the blade root (with a stress concentration factor of approximately 3.2), and the maximum deformation occurs at the blade tip. For an aluminum alloy ASHT with a diameter of 300 mm, the maximum stress and deformation for a fixed-angle configuration (60–60-60) are 2.13 MPa and 0.045 mm, respectively, whereas for a variable-angle configuration (30-45-60), they are 1.78 MPa (16.4% reduction) and 0.028 mm (37.8% reduction). (2) Fillets should be used at the blade root to mitigate stress concentration, and the blade tip thickness can be appropriately increased to reduce deformation. For TS-ASHTs with thin cross-sections, carbon-fiber-reinforced composites are recommended to enhance specific strength and stiffness, thereby preventing excessive deformation under high loads.

In riverine and near-shore sediment-laden flows, particle erosion on the blades causes increased surface roughness and changes in blade shape, ultimately degrading turbine efficiency. Figure 12 shows the erosion rate distribution of different ASHTs with different sand sizes. Song et al. [51] employed a CFD-DPM approach to systematically investigate the erosion characteristics of the ASHT and revealed the influencing trends and distribution features of the erosion rate: (1) The erosion rate is linearly related to the sand concentration: as the concentration increases from 0.4 kg/L to 1.2 kg/L, the erosion rate increases approximately twofold. This is because, under dilute-phase conditions, particle–particle interactions are negligible, and the erosion rate is primarily governed by the particle impact frequency. (2) The variation of the erosion rate with sand particle size is nonlinear: for particle sizes <0.6 mm, the erosion rate increases rapidly because small particles are easily entrained by the flow and exhibit a high impact frequency; for particle sizes >0.6 mm, the growth slows, revealing a "momentum-quantity trade-off" effect, although the momentum of a single particle increases, the number of particles per unit mass concentration decreases, resulting in a lower total impact frequency. (3) Erosion is mainly concentrated at the blade tip edge and at locations with abrupt blade curvature. For TS-ASHTs with thin cross-sections, the erosion damage is more severe because of the thinner blade leading edge; therefore, it is recommended to apply wear-resistant coatings on the blade leading edge to extend the service life.

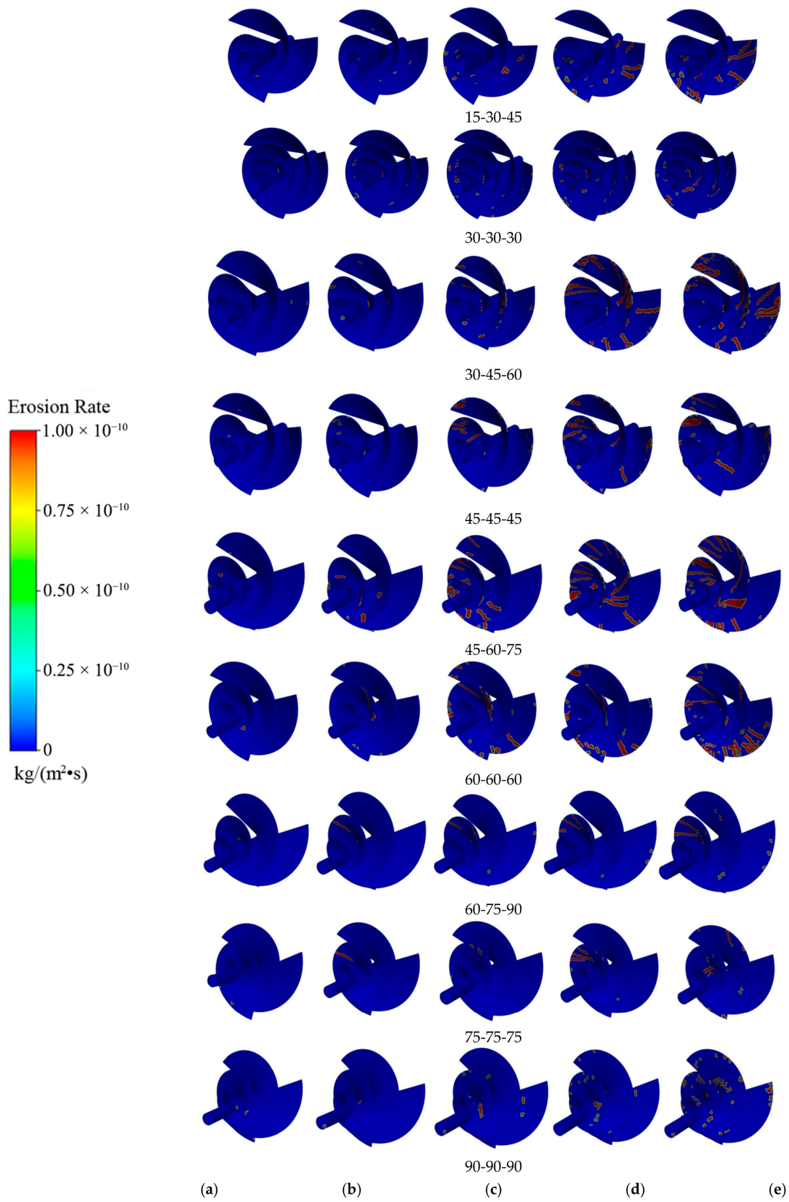

Figure 12. Erosion rate distribution of ASHTs with sand concentration of 1.0 kg/L at different sand sizes [51]: (**a**) SS = 0.2 mm; (**b**) SS = 0.4 mm; (**c**) SS = 0.6 mm; (**d**) SS = 0.8 mm; (**e**) SS = 1.0 mm.

5. Discussion

Although ASHTs have proven favorable performance in low-speed flow fields, the performance conclusions obtained from most existing laboratory tests are highly susceptible to practical operating conditions and engineering limitations.

A close examination of SL-ASHTs reveals that their widely recognized superior self-starting capability and passive yaw adaptability are highly conditional, with performance merits acutely sensitive to multiple practical factors that are often idealized in experimental settings [61]. The long shaft configuration inherent to this layout extends the transmission path and incurs extra friction loss induced by multi-point bearing supports. Nevertheless, most current self-starting experiments adopt low-friction precision bearings while ignoring the damping torque from actual generators, such as cogging torque and electromagnetic drag. As a result, the critical inflow velocity for startup and the output efficiency under low tip-speed ratios are systematically overpredicted. In field deployments, seal friction, transmission loss and generator load can substantially elevate the threshold for self-starting, potentially eroding the very low-flow advantage that defines the SL-ASHT. Compounding this uncertainty, the large axial length of SL-ASHTs amplifies wall interference effects in flume experiments, making blockage corrections far more consequential than for conventional HAHT. Widely adopted correction models such as the Pope–Harper approach were originally formulated for compact rotors, and their applicability to the three-dimensional helical long-axis geometry has not been fully validated; as noted by Zhang et al. [50], uncorrected or improperly corrected blockage effects can introduce notable deviations between laboratory-measured power coefficients and actual open-water performance, undermining the reliability of published data for engineering design. The challenge of translating laboratory findings to natural environments is further aggravated by turbulence intensity and unsteady field conditions. The passive yaw capability of SL-ASHTs has been predominantly verified under uniform steady inflow, whereas natural currents exhibit velocity fluctuations, directional shear and elevated turbulent intensities. High turbulence intensifies flow separation at the blade tip, slows the yaw response and degrades steady-state alignment accuracy, while the long-cantilevered structure becomes susceptible to flow-induced vibrations under unsteady inflow, simultaneously impairing energy harvesting efficiency and introducing structural reliability risks. Scale effects add another layer of uncertainty: most studies rely on small-scale models operating at relatively low Reynolds numbers, where boundary layer behaviour, flow separation characteristics and surface roughness sensitivity differ fundamentally from full-scale prototypes, precluding a simple extrapolation via geometric similarity. Finally, installation constraints represent a pragmatic bottleneck, as the considerable axial length imposes stringent requirements on water depth, mooring space and underwater maintenance operability, drastically reducing deployment flexibility in deep-sea platforms, narrow rivers or constrained waterways.

When attention turns to TS-ASHTs, the design narrative shifts toward structural compactness and power density, with performance enhancement measures such as ducts and blade winglets receiving extensive investigation. However, the accompanying penalties in thrust, mass, load fluctuation and fatigue are not marginal side effects but central design limitations that have not received sufficient emphasis. The most direct trade-off is the thrust amplification and its structural penalty: while ducts and winglets effectively raise the C_P. For instance, ducted ASHTs achieve a 122% increase in C_P compared with a bare rotor [52], and optimized winglets deliver a 13.7% C_P improvement [59]. They simultaneously cause a disproportionate rise in thrust coefficient, with winglet-equipped configurations exhibiting up to 17.2% higher thrust than the baseline and ducted designs generating even larger axial loads. This elevated thrust directly translates into more demanding structural requirements for support towers, mooring systems and foundations, necessitating stronger materials,

https://doi.org/10.3390/jmse14151449

heavier structures and correspondingly higher manufacturing and installation costs, so that in many practical scenarios the revenue from increased power output is partially or fully offset by the structural investment, making net economic benefit rather than maximum power coefficient the true constraint. Beyond structural loading, the increased size and mass introduced by ducts substantially expand the radial dimension and underwater weight, eroding the compactness that has distinguished ASHTs from conventional horizontal-axis turbines and raising transportation and deployment difficulty. More critically, both ducts and winglets degrade the passive yaw adaptability inherent to ASHTs: under yawed inflow, the duct inlet is prone to flow separation, causing a steeper drop in power coefficient with increasing yaw angle, while winglets aggravate circumferential load asymmetry and disrupt the self-aligning characteristic of the helical rotor. Variable-angle ASHTs already exhibit a narrower effective yaw range than fixed-angle designs, and the addition of enhancement structures further constricts the adaptive range of flow direction, rendering the turbine more vulnerable to performance degradation in environments with variable flow directions. An equally critical yet underappreciated barrier to long-term reliable operation is the intensification of load fluctuations and elevated fatigue damage risk. Unsteady analyses reveal that winglet installation increases the fluctuation amplitude of both C_P and C_D by a factor of 3.5 to 3.9 relative to the original turbine [59], and such amplified alternating loads accelerate fatigue accumulation at the blade root and tip, reducing service life and increasing maintenance frequency. For ducted ASHTs, periodic interaction between the duct wake vortex system and the rotating blades introduces additional load pulsation and associated fatigue damage. Notably, the load fluctuation behaviour of ASHTs with winglets is opposite to that of traditional lift-type horizontal-axis turbines, where winglets typically reduce load fluctuation; this unique characteristic precludes the direct transfer of structural design experience from conventional turbines. Since most existing studies prioritize average power improvement and seldom treat fatigue life and maintenance cycle as core optimization objectives, a significant gap remains between laboratory research and engineering deployment.

On the other hand, direct quantitative comparison of C_P across independent ASHT studies is compromised by systematic uncertainties rooted in geometric, operational, and methodological heterogeneities, which are especially acute when synthesizing findings from SL-ASHT and TS-ASHT. Geometric topology and operating *Re* introduce fundamental discrepancies. SL-ASHT designs, characterized by high length-to-diameter ratios and a single continuous helical blade, sustain fully developed spiral flow with limited tip leakage, whereas compact TS-ASHT configurations with three discrete blades exhibit stronger inter-blade interference and intensified tip vortex losses. Moreover, the broad spectrum of rotor diameters, blade thicknesses, hub ratios and helix angles employed in the literature yields orders-of-magnitude variation in characteristic *Re*. At the low *Re* typical of laboratory-scale models, viscous dissipation suppresses energy extraction, while full-scale high *Re* prototypes maintain more persistent boundary-layer attachment and elevated C_P, rendering direct quantitative equivalence across scales methodologically unsound. Flow blockage and its correction constitute a dominant source of bias. Experimental blockage ratios, defined as the rotor projected frontal area relative to the channel wetted cross-section, range from below 1% to nearly 40%. Elevated blockage accelerates the incident flow and artificially inflates measured power coefficients: the uncorrected maximum C_P of 0.541 reported by Rengifo et al. [40] drops to 0.407 after applying the Pope-Harper correction, corresponding to a deviation of approximately 33%. This sensitivity implies that results obtained at blockage ratios exceeding 10% cannot be directly compared with low-blockage or open-water data, a problem compounded by the diversity of correction frameworks and by the inconsistent treatment of confinement in numerical studies, where some simulations adopt unbounded domains while others replicate the exact channel geometry. Additional experimental uncertainties, torque sensor precision, unquantified mechanical friction, spatial non-uniformity of the inflow velocity profile, and velocimetry errors, further separate reported performance from intrinsic turbine behavior. Numerical simulations introduce systematic biases through choices of turbulence closure, rotor-motion formulation, and solution strategy. Relative to unsteady sliding-mesh computations, steady-state moving reference frame (MRF) simulations typically overestimate C_P by 5–8% for TS-ASHT configurations [39]. Although the SST k-ω model yields a modest mean error of about 1.37% for the average performance of a reference configuration, its predictions of wake vortex dissipation and unsteady load fluctuations deviate by more than 10%. Optimization studies add another layer of uncertainty: performance gains obtained by parametric methods such as response surface methodology (RSM) represent theoretical extrema under specific constraints rather than real operational behavior. Even when a fitting coefficient R^2 as high as 0.9814 is achieved, an RSM optimization targeting a single working condition [40] inevitably exhibits diminished benefits under variable flow conditions. Collectively, the present review therefore frames the comparison of SL-ASHT and TS-ASHT primarily around qualitative performance trends rather than absolute coefficient equivalence.

Furthermore, it is worth noting that notable uncertainties remain when extrapolating laboratory or numerical results to real ocean deployments, as most existing studies adopt uniform steady inflow conditions and neglect the multi-scale stochastic turbulent characteristics of natural marine currents. Dimitriadis et al. [62] revealed fundamental stochastic similarities between microscale turbulence and hydro-meteorological processes (wind speed and precipitation), a framework applicable to geophysical flows including ocean currents. Specifically, natural turbulent flows exhibit three distinct scaling regimes: an energy containing range at large, low-frequency scales characterized by Hurst–Kolmogorov long-range power-law dependence; an inertial subrange at intermediate scales that follows the classical Kolmogorov $-5/3$ law; and a dissipation range at small, high-frequency scales with steeper, near-exponential spectral decay. For ASHTs, multi-scale turbulence degrades performance and reliability in two primary ways: (1) High-frequency small-scale turbulence in the dissipation range intensifies boundary layer separation and tip vortex dissipation. Referring to studies on conventional horizontal-axis hydrokinetic turbines, this effect may reduce the average C_P by approximately 10–15% relative to predictions under uniform inflow. (2) Low-frequency large-scale flow fluctuations with HK long-range correlation induce periodic variations in torque and thrust, potentially increasing fatigue load amplitudes by 20–30% and elevating structural failure risk. Notably, the long-range dependence inherent in natural turbulence can produce more persistent extreme load events than predicted by standard short-memory turbulence models.

6. Conclusions

This systematic review of ASHTs under free-flow conditions reveals a fundamental shift in low-head hydropower exploitation, moving from the traditional paradigm of potential energy conversion to the direct kinetic energy capture of slow currents. The two main structural families: SL-ASHT and TS-ASHT, each exhibit distinct merits that collectively overcome the long-standing bottleneck of energy harvesting in low-velocity marine and riverine environments. The SL-ASHT, driven by the synergistic pressure difference and hydrodynamic forces along its helical passages, achieves an exceptional self-starting capability at inflow velocities as low as 0.1 m s^{-1} with a starting C_M of 0.52, and attains a maximum C_P of up to 0.51. Its passive yaw adaptability is equally striking: as the yaw angle increases from 0° to 40°, the C_P variation remains below 2%, a performance far superior to conventional HAHTs. For the TS-ASHT, compact architecture and inherently higher rotational speed enable direct coupling with generators, while best practices including variable-graded blade-angle distribution along the axis, thin airfoil profiles and non-uniform tip-gap ratios raise its maximum C_P to 0.312, with further gains achievable through ducts and winglets. These successes stem largely from multi-parameter synergistic optimization, the transfer of aerodynamic know-how from wind turbines, and the intrinsically low cut-in velocities of both configurations.

Nevertheless, the review exposes persistent weaknesses and critical knowledge gaps that temper the technology's promise. The SL-ASHT's long cantilevered shaft generates unbalanced dynamic loads, torque ripple, vibration and fatigue, risks that intensify with increasing flow speed, while its single-blade architecture challenges scalability to larger capacities. The TS-ASHT, although structurally more benign, still delivers a relatively modest maximum C_P, and its higher TSR elevates the likelihood of cavitation inception and associated noise. Performance under realistic conditions remains inadequately understood, with noticeable degradation reported under elevated turbulence intensity and strongly sheared inflows yet seldom systematically quantified. Moreover, the evidence base is almost exclusively confined to laboratory flumes and numerical simulations; long-term field data, multiphysics investigations of fluid–structure interaction, sediment erosion and biofouling, as well as cost models, life-cycle assessments and grid-integration strategies, are virtually absent, leaving the economic feasibility and operational reliability largely unvalidated.

These deficiencies translate directly into a portfolio of technical, economic and environmental risks. Fatigue failure of the long-axis and bearings of the SL-ASHT is judged to carry a moderate-to-high likelihood if left unmitigated, with severe operational consequences, while cavitation-induced blade erosion or resonance in the TS-ASHT poses a moderate risk under off-design conditions. From an application perspective, the inherently low energy density of slow currents threatens the levelised cost of energy, rendering isolated single-unit deployments economically marginal. Environmental concerns, including marine organism entanglement in un-ducted configurations and acoustic disturbance, have yet to be systematically assessed. Promising mitigation pathways do, however, emerge from the literature: the use of advanced composites and optimized bearing arrangements, real-time structural health monitoring, cavitation-resistant coatings, anti-fouling surfaces, and modular array architectures that share anchoring and electrical infrastructure can collectively reduce technical risk and lower the levelised cost of energy.

The collective experience distilled from the reviewed studies underscores several lessons. The helical flow passage is identified as the root cause of the SL-ASHT's outstanding low-velocity performance and yaw insensitivity, and successful designs consistently arise from multi-objective optimization frameworks that simultaneously balance hydrodynamic efficiency, structural integrity and manufacturability. Early underperformance frequently originated from isolating hydrodynamic optimization without accounting for axial flow gradients, blade-tip gap interactions or off-design yawed operation, revealing that the true breakthrough of ASHT technology lies in embracing a kinetic-energy rather than a potential-energy exploitation philosophy.

7. Research Avenues

Looking forward, the transition of ASHT technology from laboratory validation to engineering deployment demands a concerted, multi-pronged research agenda that moves beyond incremental improvements and embraces system-level integration. The main bottlenecks include inadequate long-term service reliability caused by sediment abrasion, cyclic fatigue and fluid-structure interaction, as well as weak adaptability to actual complex flow conditions with large yaw angles and wake interference among multiple turbines. These constraints set the scope for follow-up research. A central thrust will be the establishment of genuinely multi-parameter, multi-objective collaborative optimization frameworks. These must simultaneously balance hydrodynamic power characteristics, self-starting capability, and structural integrity to locate global optima, while critically elucidating the similarity scaling laws that bridge laboratory models and full-scale prototypes. Such design concepts can be further improved through the synergistic combination of advanced passive flow control methods inspired by the performance optimization strategies of ASWTs (vortex generators and biomimetic airfoil surfaces) and a new generation of lightweight, high-strength, wear-proof and anti-corrosion materials. In this way, the energy conversion efficiency can be elevated without sacrificing structural reliability and anti-erosion capability.

In parallel, the ability to predict and assure performance under genuine field conditions requires a leap in the fidelity of both simulation and experimental methodologies. Integrated multiphysics numerical frameworks that tightly couple fluid dynamics, structural mechanics, acoustics, and erosion processes are essential to unravel the unsteady flow structures and failure mechanisms that emerge in free-flow environments. This must be complemented by systematic experimental campaigns that depart from idealized uniform inflow, focusing instead on turbulent flows whose power-law energy spectra replicate actual hydrometeorological characteristics, bidirectional tidal currents, and wave-current coupled conditions. Only through such investigations can the quantitative deviation between idealized predictions and true long-term energy yield be rigorously assessed. Underpinning this effort is the urgent need for a unified, standardized quantitative characterization system for turbulence, employing consistent metrics such as C_P, turbulence intensity, and entropy production rate, to enable meaningful horizontal comparison of results across disparate research groups and studies.

Validating these advances requires a decisive push from laboratory flumes to full-scale, long-term field deployment. The development of kilowatt-class engineering prototypes and their sustained testing in authentic marine and riverine settings will generate the operational data essential for formulating engineering design codes, certifying performance, and defining robust operation and maintenance strategies. This real-world evidence base must be gathered alongside quantitative environmental assessments that address the interactions of ASHTs with aquatic organisms, fish, marine mammals, and invertebrates, through deliberate blade optimization to minimize collision risk and acoustic disturbance, supported by comprehensive, full-lifecycle environmental impact analyses that guarantee ecologically sustainable deployment.

Beyond the individual turbine, maximizing the energy potential of slow currents calls for holistic system and array optimization. Coordinated numerical and experimental studies must identify optimal inter-turbine spacing, rotational directions, and arrangement topologies, parallel, tandem, or triangular, to suppress wake losses and maximize the energy density of the entire array, while also exploring constructive coupling effects with complementary devices such as wave energy converters. At the system scale, the inherently low energy density of slow currents necessitates the investigation of hybrid energy integration schemes that marry ASHTs with solar photovoltaics, wave energy, and energy storage. Advancing such systems demands sophisticated, system-level design and control strategies expressly tailored to enhance supply stability and reliability for off-grid and coastal applications, thereby transforming the technology from an isolated kinetic energy harvester into a dependable, dispatchable component of a broader renewable energy infrastructure.

Author Contributions: Conceptualization, K.S.; methodology, K.S. and J.Y.; formal analysis, K.S.; investigation, K.S.; resources, K.S.; data curation, K.S.; writing—original draft preparation, K.S. and J.Y.; writing—review and editing, L.W. and Q.L.; visualization, H.H.; supervision, K.S.; project administration, K.S.; funding acquisition, K.S. All authors have read and agreed to the published version of the manuscript.

Funding: This work was supported by the Yunnan Fundamental Research Project (grant no. 202501AT070072) and the Xingdian Talent Support Program of Yunnan Province (grant no. XDYC-QNRC-2023-0159).

Data Availability Statement: No new data were created or analyzed in this study.

Conflicts of Interest: The authors declare no conflicts of interest.

References

1. Von Jouanne, A.; Agamloh, E.; Yokochi, A. A review of offshore renewable energy for advancing the clean energy transition. *Energies* **2025**, *18*, 4798. [CrossRef]
2. Li, G.; Zhu, W. Tidal current energy harvesting technologies: A review of current status and life cycle assessment. *Renew. Sustain. Energy Rev.* **2023**, *179*, 113269. [CrossRef]
3. Ma, C.; Wang, X.; Jiang, B. Ocean energy development under the background of carbon emissions peak and carbon neutrality in China. *IOP Conf. Ser. Earth Environ. Sci.* **2022**, *966*, 012003. [CrossRef]
4. Gu, Y.; Zou, T.; Liu, H.; Lin, Y.; Ren, H.; Li, Q. Status and challenges of marine current turbines: A global review. *J. Mar. Sci. Eng.* **2024**, *12*, 884. [CrossRef]
5. Lee, D.K.; Maximenko, N. Surface Drifters and Ocean Dynamics: A Review of Technological Advancements and Scientific Contributions. *Ocean Sci. J.* **2025**, *60*, 22. [CrossRef]
6. Kempton, R.C. Ocean Energy with linkages to Earth's Environmental Mechanisms, and approach to a Total Renewable Energy Structure Plan. *Jor Environ. Dyn. Geo-Sci.* **2025**, *1*, 1–24. [CrossRef]
7. Ibrahim, W.I.; Mohamed, M.R.; Ismail, R.M.T.R.; Leung, P.K.; Xing, W.W.; Shah, A.A. Hydrokinetic energy harnessing technologies: A review. *Energy Rep.* **2021**, *7*, 2021–2042. [CrossRef]
8. Mason-Jones, R.K.; Davies, P.G.; Thomas, A.J.; Griffiths, C.A. Exploring Effective Supply Chain Readiness and Resilience Within the Marine Renewable Energy Sector: A Future Reality Tree Approach. *Sustainability* **2025**, *17*, 11275. [CrossRef]
9. Copping, A.E.; Hemery, L.G.; Overhus, D.M.; Garavelli, L.; Freeman, M.C.; Whiting, J.M.; Gorton, A.M.; Farr, H.K.; Rose, D.J.; Tugade, L.G. Potential environmental effects of marine renewable energy development—the state of the science. *J. Mar. Sci. Eng.* **2020**, *8*, 879. [CrossRef]
10. Copping, A.E.; Rose, D.J.; Freeman, M.C. Moving from scientific research to consenting guidance for MRE environmental risk. In Proceedings of the 14th European Wave and Tidal Energy Conference, Plymouth, UK, 5–9 September 2021.
11. Peraza, J.I.; Horne, J.K. Quantifying conditional probabilities of fish-turbine encounters and impacts. *Front. Mar. Sci.* **2023**, *10*, 1270428. [CrossRef]
12. Rodríguez Castillo, C.A.; Yeter, B.; Li, S.; Brennan, F.; Collu, M. A critical review of challenges and opportunities for the design and operation of offshore structures supporting renewable hydrogen production, storage, and transport. *Wind Energy Sci.* **2024**, *9*, 533–554. [CrossRef]
13. Kirke, B. Towards more cost-effective river hydrokinetic turbines. *Energy Sustain. Dev.* **2024**, *78*, 101370. [CrossRef]
14. Nugraha, A.T.; Priyambodo, D. Design of hybrid portable underwater turbine hydro and solar energy power plants: Innovation to use underwater and solar current as alternative electricity in Dusun Dongol Sidoarjo. *J. Electron. Electromed. Eng. Med. Inform.* **2021**, *3*, 93–98. [CrossRef]
15. Anugrah, R.A.; Yuafiq, F.; Yusuf, M.; Peeie, M.H.B.; Yudianto, A. Computational Fluid Dynamics of Savonius Water Turbine for Hydrokinetic Pico Hydro Systems. *BIO Web Conf.* **2025**, *199*, 02009. [CrossRef]
16. Hammar, L.; Eggertsen, L.; Andersson, S.; Ehnberg, J.; Arvidsson, R.; Gullström, M.; Molander, S. A probabilistic model for hydrokinetic turbine collision risks: Exploring impacts on fish. *PLoS ONE* **2015**, *10*, e0117756. [CrossRef] [PubMed]
17. Waters, S.; Aggidis, G.A. Over 2000 years in review: Revival of the Archimedes Screw from Pump to Turbine. *Renew. Sustain. Energy Rev.* **2015**, *51*, 497–505. [CrossRef]
18. Simmons, S.C.; Lubitz, W.D. Archimedes screw generators for sustainable micro-hydropower production. *Int. J. Energy Res.* **2021**, *45*, 17480–17501. [CrossRef]
19. Kerle, H.; Mauersberger, K. From Archimedean spirals to screw mechanisms–a short historical overview. In *The Genius of Archimedes—23 Centuries of Influence on Mathematics, Science and Engineering*; Spring Nature: Berlin, Germany, 2010; pp. 163–176.
20. Khan, N.; Sarwar, M.K.; Rashid, M.; Abbasi, H.K.J.; Haider, S.; Tariq, M.A.U.R.; Nadeem, A.; Zulfiqar, M.A.; Salem, A.; Al-Ansari, N.; et al. Development of a sustainable portable Archimedes screw turbine for hydropower generation. *Sci. Rep.* **2025**, *15*, 5827. [CrossRef] [PubMed]
21. Sołowiej, P.; Łapiński, K. Recent Progress in research on the design and use of an archimedes screw turbine: A review. *Sustainability* **2025**, *17*, 201. [CrossRef]
22. Piper, A.T.; Rosewarne, P.J.; Wright, R.M.; Kemp, P.S. The impact of an Archimedes screw hydropower turbine on fish migration in a lowland river. *Ecol. Eng.* **2018**, *118*, 31–42. [CrossRef]

23. Patel, H.; Chowdhury, S. Cost effective microhydro-based microgrid schemes for rural electrification in South Africa. In *2018 53rd International Universities Power Engineering Conference*; IEEE: Piscataway, NJ, USA, 2018; pp. 1–6.
24. Montilla-López, A.I.; Velásquez-García, L.; Betancour, J.; Rubio-Clemente, A.; Chica-Arrieta, E. Performance of an Archimedes screw turbine with spiral configuration for hydrokinetic applications. *Rev. Fac. Ing. Univ. Antioq.* **2024**, *111*, 55–63.
25. Postacchini, M.; Zitti, G.; Perugini, E.; Rossetti, R.; Brocchini, M. Application of hydrokinetic turbines in microtidal rivers: The Misa River test site. *Renew. Energy* **2025**, *244*, 122634. [CrossRef]
26. Phillips, T.E.; Wood, D.H. CFD Investigation of Torque Generation in an Archimedes Screw Hydrokinetic Turbine. *Mar. Energy Res.* **2026**, *3*, 10006. [CrossRef]
27. Stergiopoulou, A.; Stergiopoulos, V.; Kalkani, E. Experimental and theoretical research of zero head innovative horizontal axis archimedean screw turbines. *Int. J. Energy Environ.* **2015**, *6*, 471.
28. YoosefDoost, A.; Lubitz, W.D. Archimedes screw turbines: A sustainable development solution for green and renewable energy generation—A review of potential and design procedures. *Sustainability* **2020**, *12*, 7352. [CrossRef]
29. Ubando, A.T.; Marfori, I.A.V., III; Peradilla, M.S.; Sy, C.L.; Calapatia, A.M.A.; Chen, W.H. Sustainable manufacturability of Archimedes screw turbines: A critical review. *J. Manuf. Mater. Process.* **2022**, *6*, 161. [CrossRef]
30. Godini, A.; Shahverdi, K.; Gohari, S. Archimedes screw turbine performance: A review. *Water Irrig. Manag.* **2023**, *13*, 1093–1105.
31. Uniyal, V.; Karn, A.; Singh, V.P. Parametric sensitivity analysis of Archimedes screw turbines for high-efficiency and sustainable hydropower. *Energy Sources Part A Recovery Util. Environ. Eff.* **2025**, *47*, 2553226. [CrossRef]
32. Abbas, Z.; Waqas, M.; Khan, S.S.; Khatoon, R.; Larkin, S.; Zhao, L. Numerical and experimental investigation of an Archimedes screw turbine for open channel water flow application. *Energy Sci. Eng.* **2024**, *12*, 1317–1336.
33. Bouvant, M.; Betancour, J.; Velásquez, L.; Rubio-Clemente, A.; Chica, E. Design optimization of an Archimedes screw turbine for hydrokinetic applications using the response surface methodology. *Renew. Energy* **2021**, *172*, 941–954. [CrossRef]
34. Zhang, D.; Guo, P.; Hu, Q.; Li, J. Parametric study and Multi-Objective optimization of a ductless Archimedes screw hydrokinetic Turbine: Experimental and numerical investigation. *Energy Convers. Manag.* **2022**, *273*, 116423. [CrossRef]
35. Zhang, D.; Guo, P.; Wang, Y.; Hu, Q.; Li, J. Influences of Yaw characteristics on the performance of an Archimedes screw hydrokinetic turbine. *Ocean Eng.* **2023**, *289*, 116307. [CrossRef]
36. Suntivarakorn, R.; Wanchat, S.; Monatrakul, W. An experimental study of electricity generation using a horizontal spiral turbine. *Energy Procedia* **2016**, *100*, 532–536. [CrossRef]
37. Monatrakul, W.; Suntivarakorn, R. Effect of blade angle on turbine efficiency of a Spiral Horizontal Axis Hydro Turbine. *Energy Procedia* **2017**, *138*, 811–816. [CrossRef]
38. Wang, B.; Wu, C.; Lv, J.; Liu, H.; Zhou, C. Performance improvement of archimedean spiral tidal current turbine based on parameter optimization. *Ocean Eng.* **2025**, *337*, 121917. [CrossRef]
39. Song, K.; Huan, H.T.; Wei, L.C.; Liu, C.X. Investigation of the effect of blade angle of Archimedes spiral hydrokinetic turbine based on hydrodynamic performance and entropy production theory. *Ocean Eng.* **2025**, *324*, 120731. [CrossRef]
40. Rengifo, J.; Velásquez, L.; Chica, E.; Rubio-Clemente, A. Optimization of the Archimedean spiral hydrokinetic turbine design using response surface methodology. *Sci* **2025**, *7*, 100. [CrossRef]
41. Puertas-Frías, C.M.; Willson, C.S.; García-Salaberri, P.A. Design and economic analysis of a hydrokinetic turbine for household applications. *Renew. Energy* **2022**, *199*, 587–598. [CrossRef]
42. Kumar, A.; Saini, G. Flow field and performance study of Savonius water turbine. *Mater. Today Proc.* **2021**, *46*, 5219–5222. [CrossRef]
43. Iliev, R.; Todorov, G.; Kamberov, K.; Zlatev, B. Evaluation of the performance of optimized horizontal-axis hydrokinetic turbines. *Water* **2025**, *17*, 1532. [CrossRef]
44. Kumar, R.; Kumar, A. Optimization of slot parameters for performance enhancement of slotted Savonius hydrokinetic turbine using Taguchi analysis. *Renew. Energy* **2024**, *237*, 121608. [CrossRef]
45. Salleh, M.B.; Kamaruddin, N.M.; Mohamed-Kassim, Z. The effects of a deflector on the self-starting speed and power performance of 2-bladed and 3-bladed Savonius rotors for hydrokinetic application. *Energy Sustain. Dev.* **2021**, *61*, 168–180. [CrossRef]
46. Zhang, D.; Chai, K.; Guo, P.; Hu, Q.; Li, J.; Shams, A. A novel full-process test bench for deep-sea in-situ power generation systems. *Energy* **2024**, *297*, 131341. [CrossRef]
47. Badawy, Y.E.; Nawar, M.A.; Attai, Y.A.; Mohamed, M.H. Co-enhancements of several design parameters of an archimedes spiral turbine for hydrokinetic energy conversion. *Energy* **2023**, *268*, 126715. [CrossRef]
48. Song, K.; Huan, H.; Kang, Y. Aerodynamic performance and wake characteristics analysis of Archimedes spiral wind turbine rotors with different blade angle. *Energies* **2023**, *16*, 385. [CrossRef]
49. Monatrakul, W.; Senawong, K.; Sritram, P.; Suntivarakorn, R. A Comparison Study of Hydro-Compact Generators with Horizontal Spiral Turbines (HSTs) and a Three-Blade Turbine Used in Irrigation Canals. *Energies* **2023**, *16*, 2267. [CrossRef]
50. Zhang, D.; Guo, P.; Cheng, Y.; Hu, Q.; Li, J. Analysis of blockage correction methods for high-solidity hydrokinetic turbines: Experimental and numerical investigations. *Ocean Eng.* **2023**, *283*, 115185. [CrossRef]

51. Song, K.; Huan, H.; Wei, L.; Wang, Y. Numerical Investigation on Erosion Characteristics of Archimedes Spiral Hydrokinetic Turbine. *J. Mar. Sci. Eng.* **2025**, *13*, 1707. [CrossRef]
52. Song, K.; Huan, H.T.; Wei, L.C.; Liu, C.X. A comparative study of hydrodynamic performance between ducted and non-ducted Archimedes spiral hydrokinetic turbines. *Ocean Eng.* **2024**, *306*, 118087. [CrossRef]
53. Kim, K.C.; Ji, H.S.; Kim, Y.K.; Lu, Q.; Baek, J.H.; Mieremet, R. Experimental and numerical study of the aerodynamic characteristics of an Archimedes spiral wind turbine blade. *Energies* **2014**, *7*, 7893–7914. [CrossRef]
54. Nawar, M.A.; Hameed, H.A.; Ramadan, A.; Attai, Y.A.; Mohamed, M.H. Experimental and numerical investigations of the blade design effect on Archimedes Spiral Wind Turbine performance. *Energy* **2021**, *223*, 120051. [CrossRef]
55. Rao, S.S.; Shanmukesh, K.; Naidu, M.K.; Kalla, P. Design and analysis of Archimedes aero-foil wind turbine blade for light and moderate wind speeds. *Int. J. Recent Technol. Mech. Electr. Eng.* **2018**, *5*, 1–5.
56. Kamal, A.M.; Nawar, M.A.; Attai, Y.A.; Mohamed, M.H. Archimedes Spiral Wind Turbine performance study using different aerofoiled blade profiles: Experimental and numerical analyses. *Energy* **2023**, *262*, 125567. [CrossRef]
57. Refaie, A.G.; Hameed, H.A.; Nawar, M.A.; Attai, Y.A.; Mohamed, M.H. Qualitative and quantitative assessments of an Archimedes Spiral Wind Turbine performance augmented by A concentrator. *Energy* **2021**, *231*, 121128. [CrossRef]
58. Hameed, H.S.A.; Hashem, I.; Nawar, M.A.; Attai, Y.A.; Mohamed, M.H. Shape optimization of a shrouded Archimedean-spiral type wind turbine for small-scale applications. *Energy* **2023**, *263*, 125809. [CrossRef]
59. Song, K.; Huan, H.; Wei, L.; Liu, C. Enhancing the Performance of Novel Archimedes Spiral Hydrokinetic Turbines Utilizing Blade Winglets in Deep-Sea Power Generation for Autonomous Underwater Vehicles. *Drones* **2025**, *9*, 72. [CrossRef]
60. Song, K.; Kang, Y. Fluid-Structure Interactions Analysis of a Drag-Type Horizontal Axis Hydraulic Turbine. *J. Phys. Conf. Ser.* **2022**, *2404*, 012001. [CrossRef]
61. Zitti, G.; Fattore, F.; Brunori, A.; Brunori, B.; Brocchini, M. Efficiency evaluation of a ductless Archimedes turbine: Laboratory experiments and numerical simulations. *Renew. Energy* **2020**, *146*, 867–879. [CrossRef]
62. Dimitriadis, P.; Koutsoyiannis, D.; Papanicolaou, P. Stochastic similarities between the microscale of turbulence and hydro-meteorological processes. *Hydrol. Sci. J.* **2016**, *61*, 1623–1640. [CrossRef]